NUREG/CR-5109
SAND88-0535

Relocation of Metallic Constituents in Core Debris Beds

Prepared by S. S. Dosanjh

Sandia National Laboratories

Prepared for
U.S. Nuclear Regulatory Commission

NOTICE

This report was prepared as an account of work sponsored by an agency of the United States Government. Neither the United States Government nor any agency thereof, or any of their employees, makes any warranty, expressed or implied, or assumes any legal liability of responsibility for any third party's use, or the results of such use, of any information, apparatus, product or process disclosed in this report, or represents that its use by such third party would not infringe privately owned rights.

NOTICE

Availability of Reference Materials Cited in NRC Publications

Most documents cited in NRC publications will be available from one of the following sources:

1. The NRC Public Document Room, 1717 H Street., N.W.
   Washington, DC 20555
2. The Superintendent of Documents, U.S. Government Printing Office, Post Office Box 37082, Washington, DC 20013-7082
3. The National Technical Information Service, Springfield, VA 22161

Although the listing that follows represents the majority of documents cited in NRC publications, it is not intended to be exhaustive.

Referenced documents available for inspection and copying for a fee from the NRC Public Document Room include NRC correspondence and internal NRC memoranda; NRC Office of Inspection and Enforcement bulletins, circulars, information notices, inspection and investigation notices; Licensee Event Reports; vendor reports and correspondence; Commission papers; and applicant and licensee documents and correspondence.

The following documents in the NUREG series are available for purchase from the GPO Sales Program: formal NRC staff and contractor reports, NRC-sponsored conference proceedings, and NRC booklets and brochures. Also available are Regulatory Guides, NRC regulations in the *Code of Federal Regulations*, and *Nuclear Regulatory Commission Issuances*.

Documents available from the National Technical Information Service include NUREG series reports and technical reports prepared by other federal agencies and reports prepared by the Atomic Energy Commission, forerunner agency to the Nuclear Regulatory Commission.

Documents available from public and special technical libraries include all open literature items, such as books, journal and periodical articles, and transactions. *Federal Register* notices, federal and state legislation, and congressional reports can usually be obtained from these libraries.

Documents such as theses, dissertations, foreign reports and translations, and non-NRC conference proceedings are available for purchase from the organization sponsoring the publication cited.

Single copies of NRC draft reports are available free, to the extent of supply, upon written request to the Division of Information Support Services, Distribution Section, U.S. Nuclear Regulatory Commission, Washington, DC 20555.

Copies of industry codes and standards used in a substantive manner in the NRC regulatory process are maintained at the NRC Library, 7920 Norfolk Avenue, Bethesda, Maryland, and are available there for reference use by the public. Codes and standards are usually copyrighted and may be purchased from the originating organization or, if they are American National Standards, from the American National Standards Institute, 1430 Broadway, New York, NY 10018.

NUREG/CR-5109
SAND88-0535
R7

Relocation of Metallic Constituents in Core Debris Beds

Manuscript Completed: July 1988
Date Published: September 1988

Prepared by
S. S. Dosanjh

Sandia National Laboratories
Albuquerque, NM 87185

Prepared for
Division of Systems Research
Office of Nuclear Regulatory Research
U.S. Nuclear Regulatory Commission
Washington, DC 20555
NRC FIN A1342

ABSTRACT

The MELPROG computer code is being developed to provide a mechanistic treatment of Light Water Reactor (LWR) accidents from accident initiation through vessel failure. This paper describes a two-dimensional (r-z) debris meltdown model that has been developed for use in the MELPROG code. Of interest in this study is melt progression in particle beds that can form in both the reactor core and the lower plenum during severe LWR accidents. The analysis includes mass conservation equations for each species. A two-dimensional (r-z) momentum equation accounts for melt relocation due to both gravity and capillary forces; viscous drag is included by modifying Darcy's Law to account for undersaturated flow, and the wetting behaviour of molten stainless steel in contact with UO_2 is modeled using the formulation suggested by Scheidegger. As solid melts in the center of the bed, the porosity increases; collapse of the bed is incorporated using a critical minimum solid volume fraction $\alpha_{s,min}$. The energy equation considers conduction and radiation heat transfer in the bed, and phase diagrams are used to model Fe-Zr and U-Zr-O interactions.

Solutions are qualitatively similar to the post-accident configuration of the Three-Mile Island (TMI-2) core. Key results are (1) a dense metallic crust is created near the bottom of the bed as molten materials flow downward and freeze; (2) liquid accumulates above the blockage and if zirconium is present, the pool grows rapidly as molten Zr dissolves both UO_2 and ZrO_2 particles; (3a) if the melt wets the solid, a fraction of the melt flows radially outward under the action of capillary forces and freezes near the radial boundary; (3b) in a nonwetting system, all of the melt flows into the bottom of the bed; and (4) when Zr and Fe are in intimate contact and the Zr atomic fraction is greater than 0.33, these metals can liquefy and flow out of the bed very early in the meltdown sequence. Major uncertainties in the analysis are identified and validation experiments are discussed.

TABLE OF CONTENTS

LIST OF FIGURES

LIST OF TABLES

NOMENCLATURE

c_p	specific heat at constant pressure [J/kg•K]
d_p	particle diameter [mm]
D	mass diffusivity [m^2/s]
g	gravitational acceleration [m/s^2]
h	enthalpy [J/kg]
h_f	heat of fusion [J/kg]
k	thermal conductivity [W/m•K]
n	particle density [particles/m^3]
P_c	capillary pressure [N/m^2]
P_g	gas pressure [N/m^2]
P_l	liquid pressure [N/m^2]
Q	decay heat [W/kg of UO_2]
r	radial distance [m]
S	saturation or liquid fraction, $\alpha_1/(\alpha_1+\alpha_g)$
S_e	effective saturation, $S_e=(S-S_r)/(1-S_r)$
S_r	residual saturation
t	time [s]
T	temperature [K]
u	liquid volumetric flux in the z direction [m/s]
U	velocity at which the solid collapses [m/s]
v	liquid volumetric flux in the r direction [m/s]
Y_{ij}	volume fraction of species j in phase i
z	distance from bottom [m]

Greek

α	volume fraction
Γ	rate of destruction of particles [particles/m^3s]
γ	surface tension [N/m]
ϵ	emissivity
θ	liquid-solid contact angle [°]
κ	permeability [m^2]
μ	viscosity [Pa•s]
ρ	theoretical density [kg/m^3]

Subscripts

g	gas
l	liquid
s	solid

1. INTRODUCTION

1.1 Problem of Interest

The MELPROG computer code [1-3] is being developed to provide a mechanistic treatment of Light Water Reactor (LWR) accidents from accident initiation through vessel failure. The MELPROG code is organized into explicitly linked modules that analyze different aspects of a severe accident. At the beginning of an accident, heat transfer in the reactor core is calculated in the CORE module. Once the fuel rods fragment, the core resembles a large particle bed. From this point in time onward, core melt progression is calculated in the DEBRIS module (dryout, quenching and gas flow in the bed are modeled in the FLUIDS module). The DEBRIS module also analyzes beds that can form in the lower plenum.

This paper describes models that are being developed for the DEBRIS module and discusses experimental needs in this area. Of interest in this study is the transition of an initially dry particle bed to a molten pool state. Although the energy released by fission product decay falls to less than one-percent of normal operating power one hour after reactor shutdown [4], temperatures in a dry debris bed can surpass the UO_2-ZrO_2 melting point (2800 K) due to the low UO_2 and ZrO_2 thermal conductivities [5]. When the solid debris starts melting, molten materials flow downward under the action of gravity and freeze in lower, colder portions of the bed, forming a dense crusted region. As happened at Three-Mile Island (TMI-2), liquid subsequently accumulates above this crust, creating a molten pool [6-8]. Postaccident analyses of the TMI-2 reactor core revealed that debris was released into the lower plenum of the reactor vessel when the supporting crust failed.

1.2 Related Studies

Because uncoolable, dry debris represents a significant risk, the dryout [5,9-26], quenching and reflooding [27-31] of internally heated particle beds has received considerable attention in the literature. Squarer et al.[10] and Lipinski [11] have presented reviews of recent debris coolability research. Lipinski [12] elucidated much of the physics involved in dryout and developed a steady, one-dimensional model that successfully predicted dryout limits. Time-dependent models were subsequently developed by E. Gorham-Bergeron [13] and Turland and Moore [14,15]. Reactor D-series [16-22] and Degraded Core Coolability [23-24] experiments at Sandia National Laboratories investigated debris dryout in Liquid Metal Fast Breeder Reactors (LMFBR) and Light Water Reactors (LWR), respectively. Related experiments were conducted by Dhir and Catton [25] and Squarer and Peoples [26].

Natural convection effects in the molten pool state have been investigated in many LMFBR studies [32-39]. Emara and Kulacki [32], Suo-Anttila and Catton [33], Cheung [34] and Tveitereid [35] modeled natural convection flows in horizontal fluid layers with internal energy generation. Kulacki and Goldstein [36], Baker et al.[37] and Faw et al.[38] present experimental correlations for upward and downward heat partitioning in such fluid layers.

Relatively little attention has been given to the postdryout meltdown of debris beds that form during LWR accidents [40]. Several Melt Progression (MP) experiments are being planned at Sandia National Laboratories to investigate (1) the transition of a dry LWR debris bed to a molten pool state and (2) the failure of the supporting crust. These experiments will be performed in the Annular Core Research Reactor at Sandia and are intended to complement earlier Molten Pool [41-45] and Dry Capsule [46-47] experiments which investigated incipient debris melting within the context of LMFBR accidents. The importance of U-Zr-O chemistry will be examined in the MP experiments whereas the earlier LMFBR work stressed UO_2-stainless steel interactions. Larger particles will be used in the MP study (average diameters near 2 mm versus 0.2 mm in the DC experiments) and the temperature gradients will be smaller. Because of the large thermal gradients in the DC experiments, evaporation and recondensation was a dominant crust formation process [47].

1.3 The Present Contribution

The present study is an extension of earlier work by Dosanjh [48-50]. A mechanistic, one-dimensional model was presented in Refs.[48,49] for the postdryout meltdown of UO_2-ZrO_2 beds. The analysis included mass conservation equations for each species. A momentum equation accounted for melt relocation due to both gravity and capillary forces; viscous drag was included by modifying Darcy's Law to account for undersaturated flow. A UO_2-ZrO_2 phase diagram was prescribed and the energy equation considered conduction and radiation heat transfer in the bed and convection by the melt. A two-dimensional debris meltdown model [50] was subsequently developed to treat reactor accidents, such as TMI-2, during which multidimensional effects have an important impact on core melt progression.

In this report, metals (e.g. zirconium and stainless steel) are added to the two-dimensional version of the analysis. The wetting behavior of molten stainless steel in contact with solid UO_2 is modeled using the formulation suggested by Scheidegger [51]. A Zr-Fe phase diagram accounts for the formation of a low temperature (≃1200 K) liquid solution and the dissolution of solid UO_2 and ZrO_2 by molten Zr is considered using a quasi-equilibrium treatment. A nonoxidizing atmosphere is prescribed in this study: calculations using the MELPROG code [2] indicate that this is a reasonable approximation during the late phases of many severe accident sequences. The oxidation of zirconium and stainless steel will be considered in future reports.

A discussion of the analysis follows. Solutions are presented in Chapter 3 for porous beds with several compositions: (1) UO_2, ZrO_2 and Zr; (2) UO_2 and stainless steel; and (3) UO_2, ZrO_2, Zr and Fe. The effects of varying $\alpha_{s,min}$ (the solid fraction at which the bed collapses) and the liquid-solid contact angle θ are discussed. Major uncertainties in the analysis are identified and validation experiments are discussed. These experiments are of critical importance because uncertainties in the debris module can affect reactor accident analyses; such uncertainties can alter the manner in which core materials are released into the lower plenum, the state of the lower plenum debris and the timing of both core slump and vessel failure.

2. ANALYSIS

The distance characteristic of changes in the pore structure of the debris bed d_p is defined as six times the volume of the solid phase divided by its surface area (i.e. $d_p=6V/A$). The equations governing heat transfer and fluid flow in the bed are amenable to analysis for a particular range of d_p. When d_p is on the order of the mean free path of the gas molecules λ, corresponding to the Knudsen limit, the diffusion models employed in this study must be modified. On the other hand, when d_p is large, of the same order as x_c, the distance characteristic of changes in temperature and species concentrations, the particles must be considered individually. The following analysis is restricted to debris beds in which d_p satisfies $\lambda << d_p << x_c$.

2.1 Conservation of Mass

Balancing the mass stored in a control volume and convection by the liquid and the solid (as it collapses) gives:

$$\frac{\partial}{\partial t}\left[\alpha_1 Y_{1j}\rho_{1j}\right] + \bar{\nabla}\cdot\left[Y_{1j}\rho_{1j}\bar{u}\right] + \frac{\partial}{\partial z}\left[\alpha_s Y_{sj}\rho_{sj}U\right] = -\frac{\partial}{\partial t}\left[\alpha_s Y_{sj}\rho_{sj}\right] \quad , \qquad (1)$$

for each species j; j=1,2,3 and 4 corresponding to UO_2, ZrO_2, Zr and stainless steel, respectively. The subscripts 1 and s refer to liquid and solid, respectively, $\bar{u}=(u,v)$ is the liquid superficial velocity, U is the velocity at which the solid collapses, α is a volume fraction and Y_{ij} is the volume fraction of phase i that is occupied by species j.

Note that species diffusion is neglected in Eq.(1). Typical diffusivities for liquids near their melting points are on the order of 10^{-9} m^2/s [52]. For time scales on the order of 10^3 s, the distance characteristic of diffusion, $[Dt]^{1/2}$, is approximately 10^{-3} m. That is, liquid phase diffusion is only important over length scales comparable to the average particle diameter.

2.2 Liquid Motion

Balancing viscous drag (which is assumed to vary linearly with velocity), gravity and changes in pressure gives:

$$\rho_1 \frac{\partial \bar{u}}{\partial t} + \frac{\mu}{\kappa_1} \bar{u} = - \bar{\nabla} P_1 - \bar{g} \rho_1 \qquad , \tag{2}$$

where μ is the dynamic viscosity of the liquid, g is the gravitational acceleration and κ_1 is the relative permeability. Capillary forces enter Eq.(2) through the term involving the liquid pressure, P_1. The capillary pressure is defined as the difference between P_1 and the gas pressure, P_g (that is, $P_c=P_g-P_1$) [51,53-55]. Taking changes in the gas pressure to be much smaller than variations in the capillary pressure ($\nabla P_g << \nabla P_c$) gives $\nabla P_1 = -\nabla P_c$. From Eq.(2) it is therefore evident that capillary forces move liquid into regions of high P_c.

In order to solve Eq. (2) the relative permeability κ_1 and the capillary pressure P_c must be specified. In fully saturated flow, κ_1 equals the permeability κ, while in undersaturated flow, only a fraction of the solid is in contact with liquid and κ_1 is proportional to κ; the proportionality constant is a function of the saturation S which is defined as the fraction of nonsolid volume occupied by liquid (i.e. $S=\alpha_1/(\alpha_1+\alpha_g)$). Reed [22] gives for κ_1:

$$\kappa_1 = \begin{cases} \kappa S_e^3 & , \text{ for } S>S_r \\ 0 & , \text{ for } S \leq S_r \end{cases} \tag{3}$$

where $S_e=(S-S_r)/(1-S_r)$ and the residual saturation S_r is defined as the threshold value of saturation below which bulk liquid motion ceases. For $S \leq S_r$, $\kappa_1=0$ and Eq.(2) requires that $\bar{u}=0$. When the saturation S is less than the residual saturation S_r, the liquid consists of unconnected pendular rings. Liquid starts to flow when S is increased to the point that these rings touch and coalesce [56]. When the liquid wets the solid ($0° < \theta < 90°$),

$$S_r = \frac{1}{86.3} \left[\frac{\gamma \cos\theta}{\kappa \rho_1 g} \right]^{0.263} \quad , \tag{4}$$

where γ is the surface tension and θ is the liquid-solid contact angle [57]. In a nonwetting system ($90° < \theta < 180°$), $S_r = 0.0$. The dependence of S_r on the porous matrix is contained in the permeability κ. Increasing the particle diameter or the porosity raises κ and leads to lower values of S_r. For packed beds consisting of small, tightly packed particles, the saturation must be increased to a high value before bulk liquid motion is observed. Bird [58] derives the following relation for κ by modeling the porous solid as a bundle of capillary tubes:

$$\kappa = \frac{d_p^2 \, \epsilon^3}{150 \, (1-\epsilon)^2} \quad , \tag{5}$$

where the factor of 150 is determined empirically.

Leverett [56] derived the following equation for the capillary pressure P_c using dimensional analysis: $P_c = J \, \gamma \cos\theta \, (1-\alpha_s)^{1/2} / \kappa^{1/2}$, where J is a function of S_e only. Hoffman and Barleon [59] give an empirically determined relation for J: $J = a \, (S_e + b)^{-c}$, where $a=0.38$, $b=0.014$ and $c=0.27$. Therefore,

$$P_c = a \, (S_e + b)^{-c} \, \gamma \cos\theta \, \frac{\sqrt{150} \, \alpha_s}{d_p (1-\alpha_s)} \quad . \tag{6}$$

Because P_c decreases as the particle diameter d_p increases, capillary forces are small in beds with large particles. For $0° < \theta < 90°$, increasing the solid fraction α_s or decreasing the saturation S_e increases P_c; capillary forces therefore move liquid into regions of high α_s (low porosity) and low saturation. For $90° < \theta < 180°$, decreasing α_s or increasing S_e increases P_c; capillary forces therefore move liquid into regions of low α_s (high porosity) and high saturation. That is, melt tends to agglomerate in a nonwetting system. This effect has been observed in stainless steel-UO_2 beds in both the Molten Pool and Dry Capsule experiments.

2.3 Solid Motion

In order to determine the solid velocity U, the manner in which a high porosity bed collapses must be specified. It is assumed here that solid begins collapsing downward when the solid fraction falls below a critical value $\alpha_{s,min}$ and that $\alpha_s=\alpha_{s,min}$ in regions into which solid is collapsing. That is, U is determined by requiring enough solid to fall to keep the solid volume fraction above this minimum value.

The particle density n is determined from

$$\frac{\partial n}{\partial t} + \frac{\partial}{\partial z} nU = \Gamma \quad , \tag{7}$$

where Γ is the rate of destruction by phase changes. After solving Eq.(7) for n, the particle diameter is determined from $d_p=(6\alpha_s/n\pi)^{1/3}$.

2.4 Gas Motion

When the models discussed in this study are coupled to the MELPROG computer code, gas motion will be calculated in the FLUIDS module of the code. In the near future, a gas phase momentum equation and gas species diffusion equations will be added to the stand-alone version of the current debris bed meltdown model. Gas motion can affect both oxidation and fission product release in debris beds. In the present study it is assumed that oxidation ceases when the core suffers a significant loss of geometry.

2.5 Conservation of Energy

Balancing the energy stored in the solid and the liquid, convection by the liquid and the solid (as it collapses), diffusion and internal heat generation gives:

$$\frac{\partial}{\partial t} \sum_j \left[\alpha_s Y_{sj}\rho_{sj}h_{sj} + \alpha_l Y_{lj}\rho_{lj}h_{lj}\right] + \overline{\nabla}\cdot\left[\overline{u} \sum_j Y_{lj}\rho_{lj}h_{lj}\right]$$

$$+ \frac{\partial}{\partial z}\left[\alpha_s U \sum_j Y_{sj}\rho_{sj}h_{sj}\right] = \overline{\nabla}\cdot k_{eff}\overline{\nabla}T + \left[\alpha_s\rho_{s1}Y_{s1} + \alpha_l\rho_{l1}Y_{l1}\right]Q, \tag{8}$$

where h_{ij} is the enthalpy of species j in phase i, Q is the decay heat expressed as energy release per mass of UO_2 and k_{eff} is an effective thermal conductivity which accounts for both conductive and radiative heat transfer in the porous solid. It is assumed here that the liquid and the solid are in local thermal equilibrium. Energy stored in the gas phase is neglected because the densities of materials of interest are very large (on the order of 10^4 kg/m^3) compared with the gas density.

Radiation heat transfer in the packed bed is incorporated using a modified gas conductivity, $k_g^* = k_g + k_{rad}$, where $k_{rad} = 4\epsilon\sigma d_p T^3$, ϵ is the emissivity of the solid and σ is the Stefan-Boltzmann constant [60,64]. Empirical correlations for k_{eff} in solid-gas systems are available in the literature [60-64]. However, in the current problem, three phases (solid, liquid and gas) are present. In calculating k_{eff}, the solid and the liquid are treated as a single component with a volume averaged thermal conductivity k_σ:

$$k_\sigma = \frac{1}{\alpha_s + \alpha_1} \left[\alpha_s \sum_j Y_{sj} k_{sj} + \alpha_1 \sum_j Y_{1j} k_{1j} \right] \tag{9}$$

For a single phase i, k_σ depends only on Y_{ij} and k_{ij}. The following correlation gives k_{eff} [60,64]:

$$k_{eff} = \psi k_g^* + \frac{1-\psi}{k_\sigma \omega + k_g^*(1-\omega)} k_\sigma k_g^* \quad , \tag{10}$$

where $\omega = 0.3\alpha_g^{1.8}(k_s/k_g^*)^{-0.044}$, $\psi = (\alpha_g - \omega)/(1-\omega)$ and α_g is the volume fraction occupied by gas. In the limit of a gas volume fraction of zero, both ω and ψ approach zero and consequently, $k_{eff} = k_\sigma$. On the other hand, in the limit of a gas volume fraction of one, ψ approaches one and $k_{eff} = k_g^*$.

2.6 Phase Diagrams

At the present time, reaction rate information is not available in the literature for the materials and temperatures of interest. Consequently, quasi-equilibrium treatments based on relevant phase diagrams are used in this study to model Fe-Zr and U-Zr-O interactions. Shown in Fig. 1 is the Zr-Fe phase diagram given by Hansen [65]. Note that solid melts at a very low temperature for Zr atomic fractions greater than 0.33; when the temperature reaches 1200 K, a eutectic reaction occurs forming a Zr-Fe liquid solution having a Zr fraction of 0.76. For Zr

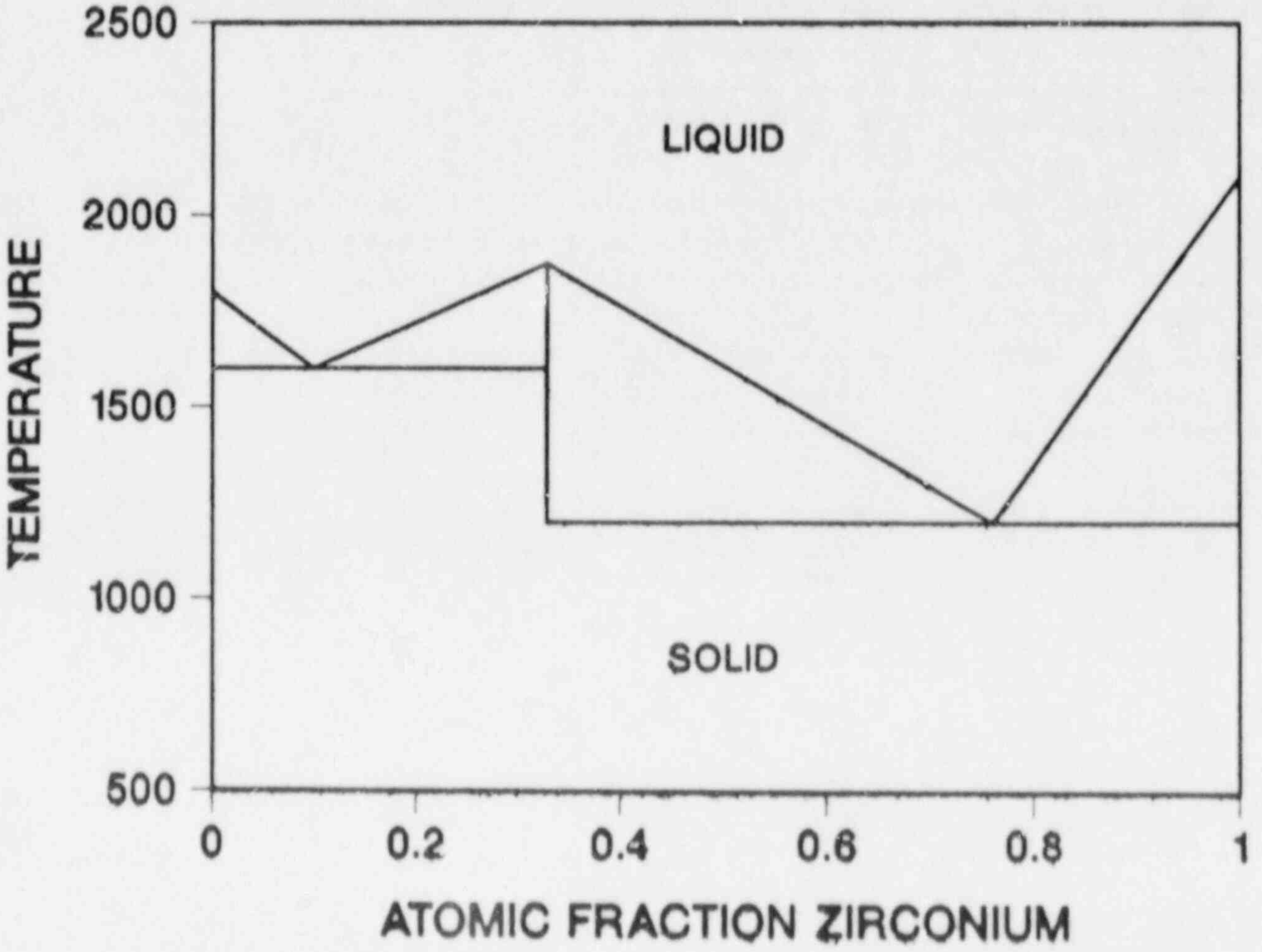

FIG. 1: Zr–Fe phase diagram.

atomic fractions between 0.33 and 0.76, this eutectic reaction decreases the Zr atomic fraction in the solid phase to 0.33. That is, a solid $ZrFe_2$ compound is created. For Zr atomic fractions between 0.76 and 1.0, the reaction increases the Zr fraction in the solid to 1.0 (all of the Fe liquefies). Because of the low solidification temperature (1200 K) of the Zr-Fe solution, only a small fraction will freeze near the bottom of the bed; most of the melt flows out of the bed very early in the meltdown sequence. This phenomenon is discussed further in Sections 3.3a and 3.3b.

When the temperature surpasses 2100 K, molten Zr dissolves both UO_2 and ZrO_2 [66,67]. In this study these dissolution processes are taken to be symmetric with respect to UO_2 and ZrO_2 compositions. For a given local (solid and liquid) composition, it is assumed that the melt composition falls along the line shown in Fig. 2. The solubilities of UO_2 and ZrO_2 in molten Zr are computed from the U-Zr-O liquidus temperature.

Although Zr-UO_2, Zr-ZrO_2 and ZrO_2-UO_2 pseudo binary phase diagrams are available in the literature [66,67], a ternary U-Zr-O phase diagram is not available. Ternary liquidus temperatures are determined in this study following the interpolation method suggested in Ref. [68]:

$$T_L = \frac{\sum\limits_{\substack{i,j \\ i\neq j}} f_i f_j T_{Lij}}{\sum\limits_{\substack{i,j \\ i\neq j}} f_i f_j} , \tag{11}$$

where the f's are atomic fractions and T_{Lij} is the liquidus temperature for the i-j binary phase diagram. Equation (11) correctly reduces to $T_L = T_{Lij}$ when only two components are present. Liquidus temperatures currently used in the MELPROG computer code are given in Tables IA, IB and IC.*

---

*Private communication with R.C. Smith, Sandia National Laboratories, Reactor Safety Theoretical Physics Division, 1988.

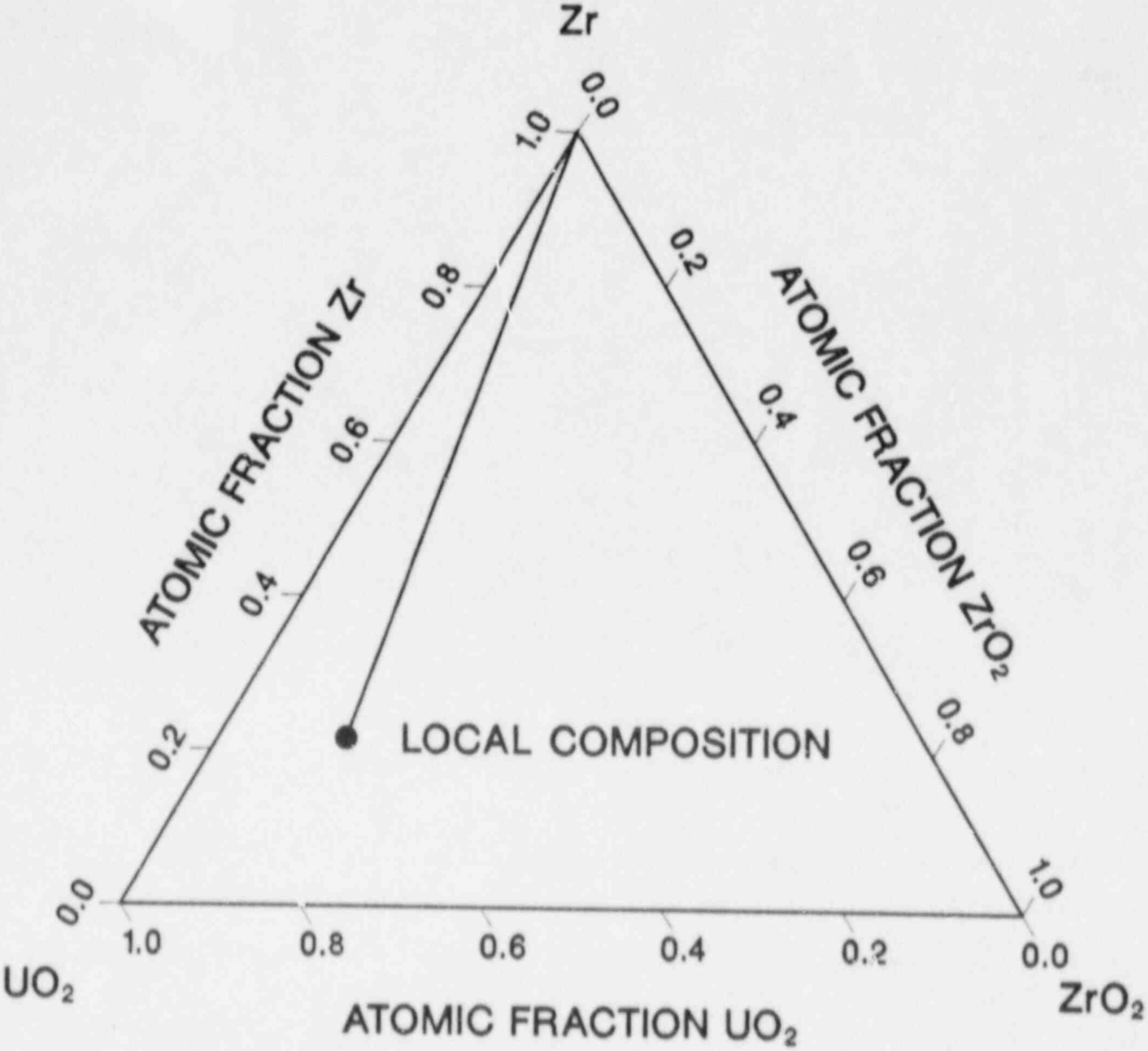

FIG. 2: Possible melt compositions for a mixture with the local composition (solid and liquid) shown.

TABLE IA

Liquidus temperatures for $Zr-UO_2$. The quantity f_{UO2} is the UO_2 molecular fraction.

Temperature		Range of molecular fractions
$T_L =$	$2100 + 1460 f_{UO_2}$	for $0.000 < f_{UO_2} < 0.050$
	$2173 + 2841 (f_{UO_2} - 0.05)$	for $0.050 < f_{UO_2} < 0.226$
	$2673 + 1.6 (f_{UO_2} - 0.226)$	for $0.226 < f_{UO_2} < 0.856$
	$2674 + 3049 (f_{UO_2} - 0.856)$	for $0.856 < f_{UO_2} < 1.000$

TABLE IB

Liquidus temperatures for $Zr-ZrO_2$. The quantity f_{ZrO2} is the ZrO_2 molecular fraction.

Temperature		Range of molecular fractions
$T_L =$	$2100 + 210 f_{ZrO_2}$	for $0.000 < f_{ZrO_2} < 0.347$
	$2173 + 1225 (f_{ZrO_2} - 0.347)$	for $0.347 < f_{ZrO_2} < 1.000$

TABLE IC

Liquidus temperatures for ZrO_2-UO_2. The quantity f_{UO2} is the UO_2 molecular fraction.

Temperature	Range of molecular fractions
$T_L = \begin{cases} 2973 - 336\, f_{UO_2} \\ 2805 + 616\, (f_{UO_2} - 0.5) \end{cases}$	for $0.0 < f_{UO_2} < 0.5$ for $0.5 < f_{UO_2} < 1.0$

2.7 Closure

In order to close the preceding set of equations, the decay heat Q, properties, initial conditions and boundary conditions must be specified. One hour after reactor shutdown, power generation falls to approximately one percent of peak power [4]. A TMI-2 type plant with an operating power of 2.8×10^3 MW and 93,000 kg of UO_2 in the core [7] has a decay heat Q on the order of 300 W/kg of UO_2. Because it takes several days for the decay heat to decrease significantly below the one-hour value [4], it is assumed that Q is constant in the following analysis.

Typical values of densities ρ_{ij}, specific heats c_{pij}, heats of fusion h_{fj}, thermal conductivities k_{ij}, viscosities μ_j and surface tensions γ_j for UO_2 [69-71], ZrO_2 [72], Zr [66], stainless steel [72] and Fe [73] are given in Table II. Initial measurements of the liquid UO_2 thermal conductivity ranged from 2.0 W/m•K to 11.0 W/m•K [74,75]. Upon subsequent analysis of these experiments, Fink and Leibowitz [76] suggested a value of 5.5 W/m•K. The gas is taken to be hydrogen, for which $k_g = 1.097 \times 10^{-3}\, T^{0.8785}$, where k_g is measured in W/m•K and T is in Kelvins [66]. The viscosity of the melt is calculated by volume averaging. Brimhall and Prater [77] noted that the dissolution of UO_2 by molten Zr is a weakly exothermic process; this heat of reaction is set equal to zero in this study.

TABLE II

Typical UO_2, ZrO_2, Zr, 304 stainless steel and Fe properties.

Property	UO_2	ZrO_2	Zr	304 steel	Fe
density [kg/m^3]	9650 (s) 8700 (l)	5700 (s) 5700 (l)	6400 (s) 6200 (l)	7500 (s) 6900 (l)	7900 (s) 7900 (l)
specific heat [J/kg-K]	630 (s) 490 (l)	700 (s) 815 (l)	350 (s) 350 (l)	560 (s) 560 (l)	780 (s) 750 (l)
thermal conductivity [W/m-K]	3.0 (s) 5.5 (l)	2.0 (s) 2.7 (l)	30.0 (s) 35.0 (l)	30.0 (s) 20.0 (l)	30.0 (s) 30.0 (l)
heat of fusion [kJ/kg]	274.0	706.0	225.0	250.0	290.0
viscosity [Pa-s]	0.0058	0.0035	0.0050	0.0225	0.0225
surface tension [N/m]	0.45	0.45	0.45	1.5	1.8

Solutions are presented in Section 3 for various initial and boundary conditions. When the models discussed in this study are explicitly coupled to the MELPROG code, these conditions will be calculated in other modules of the code. For example, initial bed compositions will be provided by the CORE module; this module calculates heat transfer in the reactor core during the early stages of a reactor accident. Boundary conditions will be provided by either the STRUCTURES or CORE modules for boundaries that are in contact with reactor structures and by the RADIATION module when radiative boundary conditions are appropriate.

2.8 Solution Algorithm

Equations (1,2 and 10) along with auxiliary relations (3-9) are solved numerically. Variables such as the temperature and the species volume fractions are determined at the centers of the computational cells. Velocities are calculated at the sides of these cells. Results presented in Section 3 were obtained using 200 computational cells; increasing this number did not significantly alter the solutions.

Given the values of all variables at a time step n, Eq.(2) is solved for the velocity field at step n+1; the velocity in the drag term is evaluated implicitly and all other parameters are determined explicitly. Next, the bulk densities (which are based on total volume),

$$\tilde{\rho}_j = \alpha_s Y_{sj} \rho_{sj} + \alpha_l Y_{lj} \rho_{lj} \quad , \qquad (12)$$

and the enthalpy function,

$$H = \sum_j \left[\alpha_s Y_{sj} \rho_{sj} h_{sj} + \alpha_l Y_{lj} \rho_{lj} h_{lj} \right] \quad , \qquad (13)$$

are calculated at time step n+1 from Eqs.(1,10) using a time explicit scheme; convective terms in these equations are evaluated using upwind differencing. When only one phase is present, solution of Eqs.(1,10) is straightforward. In two phase regions, phase diagrams provide additional relations between the temperature and the species mole fractions in each phase. Equations (12,13) along with these phase diagram relations determine the primitive variables, T, α_i, and Y_{ij}, at step n+1.

3. RESULTS AND DISCUSSION

Solutions are presented in the following sections for a 1 m high, 1 m in diameter porous bed composed of particles with an initial average diameter of 5 mm. An initial uniform temperature of 600 K is prescribed and the boundaries continue to radiate to an environment at 600 K as the temperature increases due to decay heating. The following compositions are considered: (1) UO_2, ZrO_2 and Zr; (2) UO_2 and stainless steel; and (3) UO_2, ZrO_2, Zr and Fe. Although nonhomogeneous initial and boundary conditions can be prescribed, uniform conditions are chosen to simplify the interpretation of the results. When the models discussed in this study are implemented in the MELPROG code, the initial state of the debris and the boundary conditions will be calculated for each problem of interest.

3.1a CASE 1A: Zirconium in a Ceramic Bed with $\alpha_{s,min}=0.4$J1420

Solutions are presented in this section for a bed with initial U02, Zr02 and Zr volume fractions of 0.33, 0.07 and 0.20, respectively, and an initial porosity of 0.4 -- see Fig. 3. In this section it is assumed that solid begins collapsing downward when the solid volume fraction falls to $\alpha_{s,min}=0.4$. The effect of varying $\alpha_{s,min}$ is discussed in Section 3.1b.

Temperature, porosity, solid volume fraction and centerline species profiles at 4600 s are shown in Figs. 4,5,6 and 7, respectively. When the temperature surpasses 2100 K, the Zr melts, decreasing the solid fraction in the center of the bed. Most of the melt flows downward and freezes upon reaching colder portions of the bed; note from Figs. 6 and 7 that a metallic blockage forms near the bottom of the bed. A small fraction of the melt flows radially outward under the action of capillary forces and freezes near the radial boundary.

Shown in Fig. 8 is the temperature profile at 5700 s. Temperatures in the bed are well above 2100 K and significant amounts of UO_2 and ZrO_2 have been dissolved by molten Zr. As happened at Three-Mile Island (TMI-2), liquid accumulates above the metallic blockage, creating a two phase (liquid-solid) molten pool -- see Figs. 9,10 and 11. Recall that the minimum allowable solid volume fraction in this calculation is 0.4 and that the

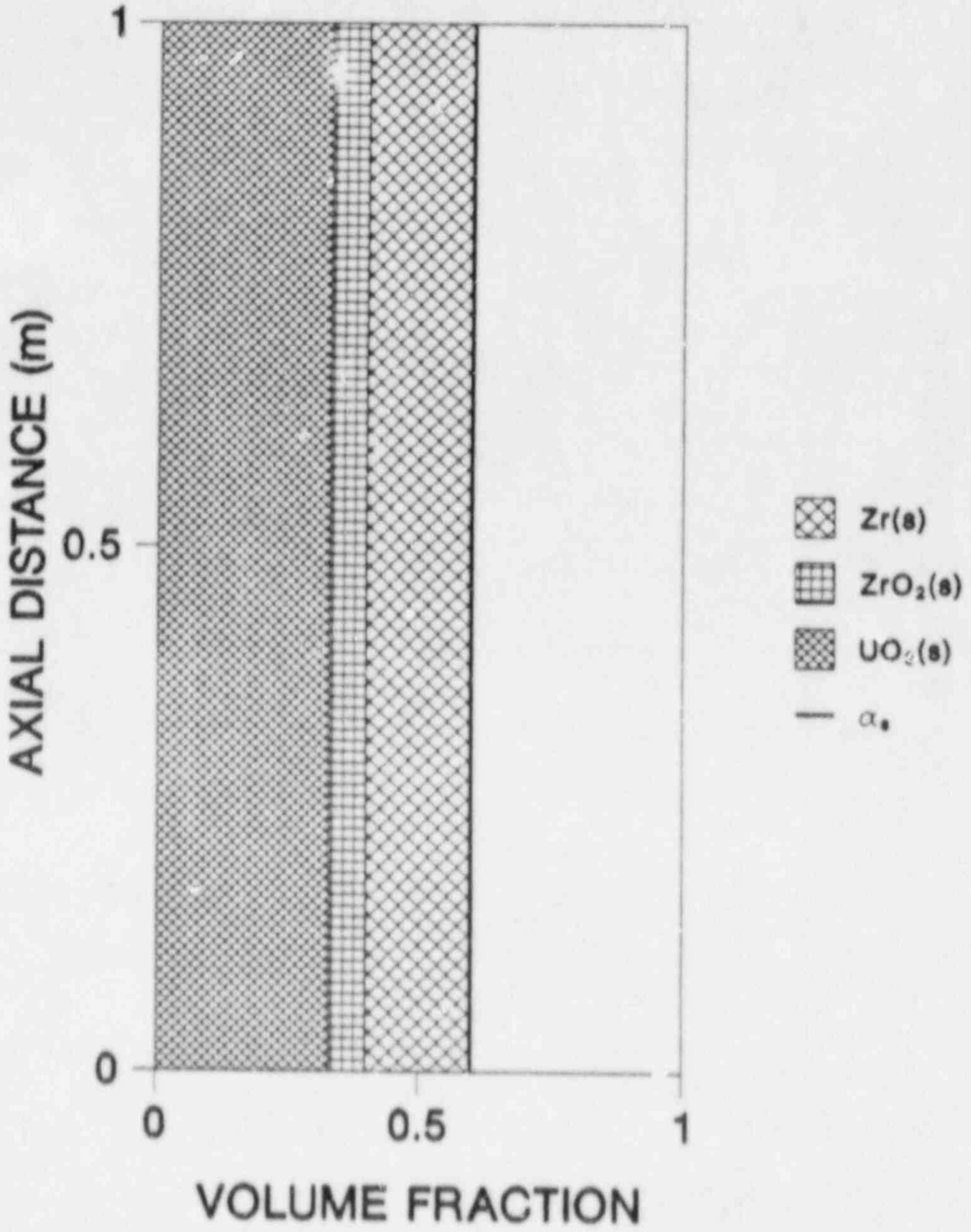

FIG. 3: Initial species volume fractions for Cases 1a and 1b.

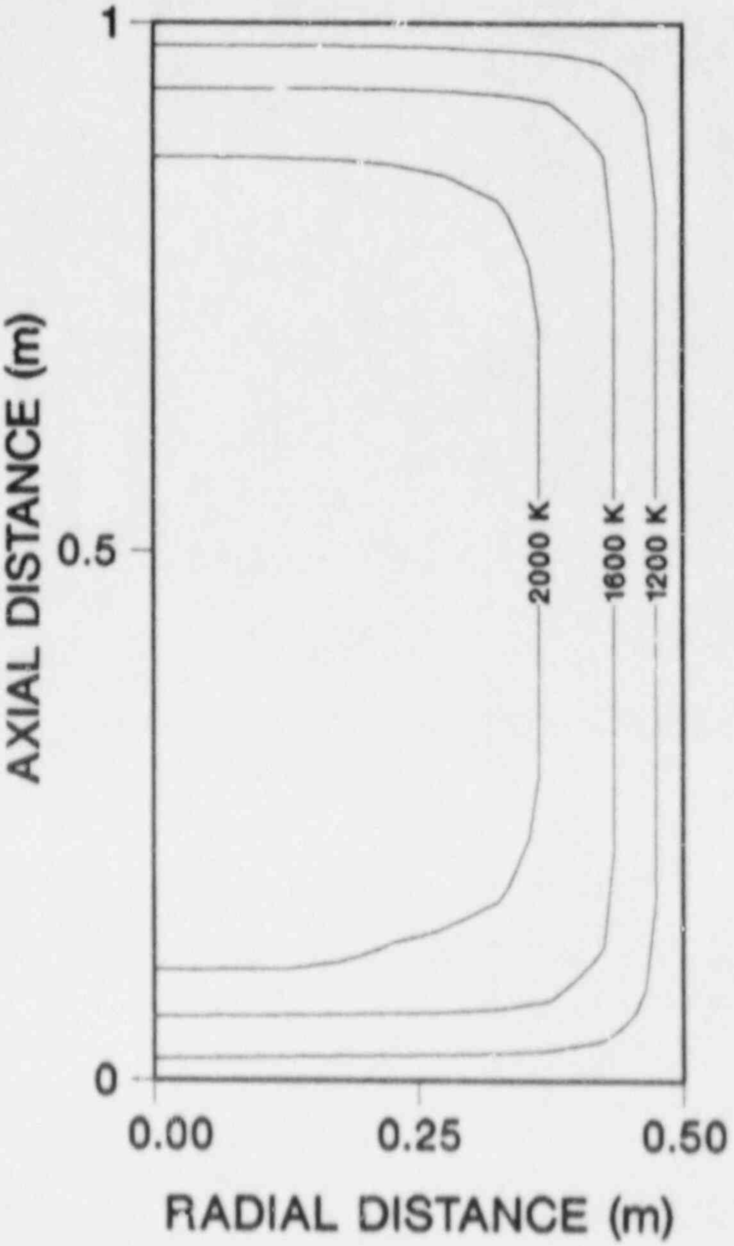

FIG. 4: Temperature contours at t=4700 s for Case 1a.

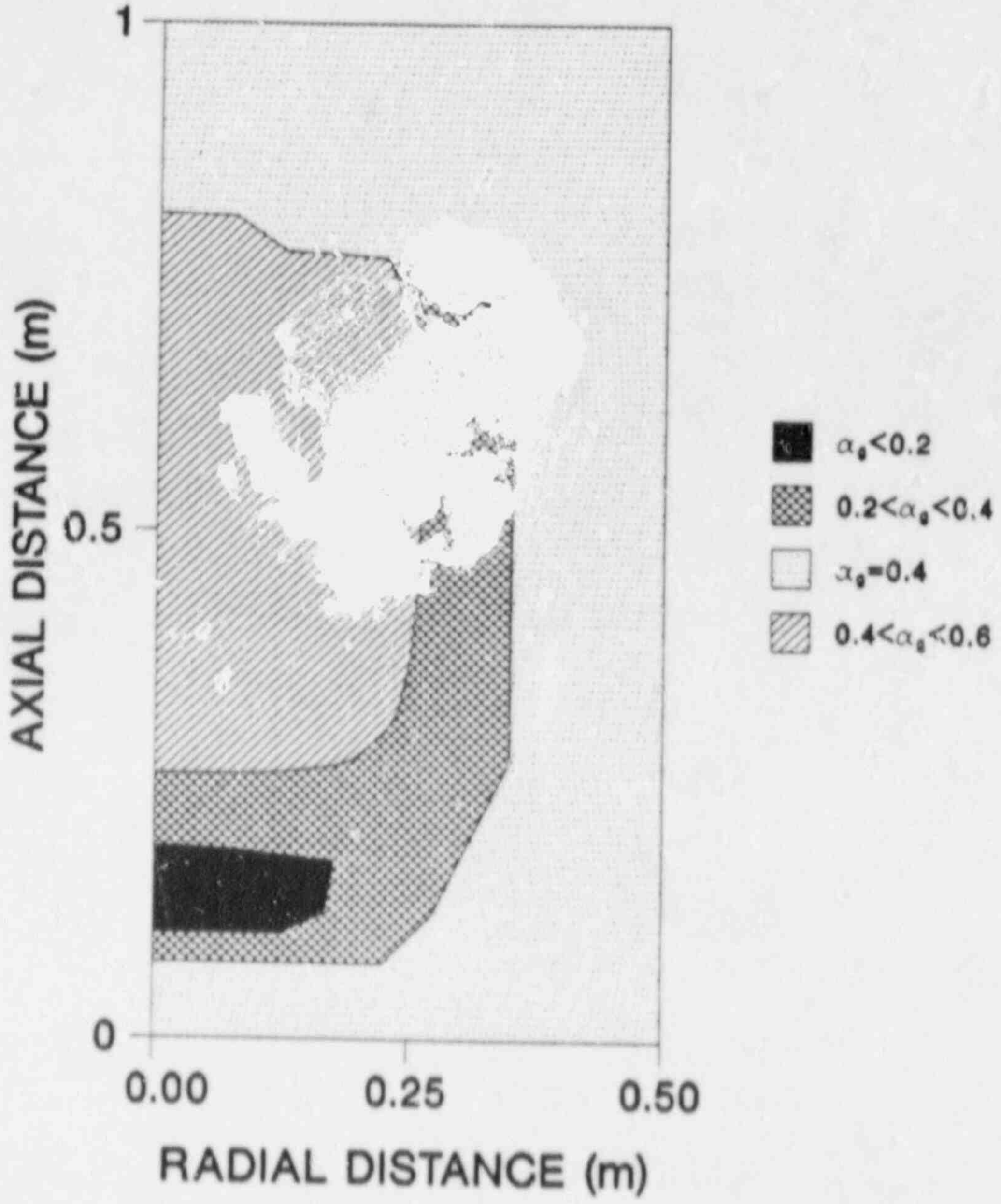

FIG. 5: Gas volume fraction α_g at t=4700 s for Case 1a.

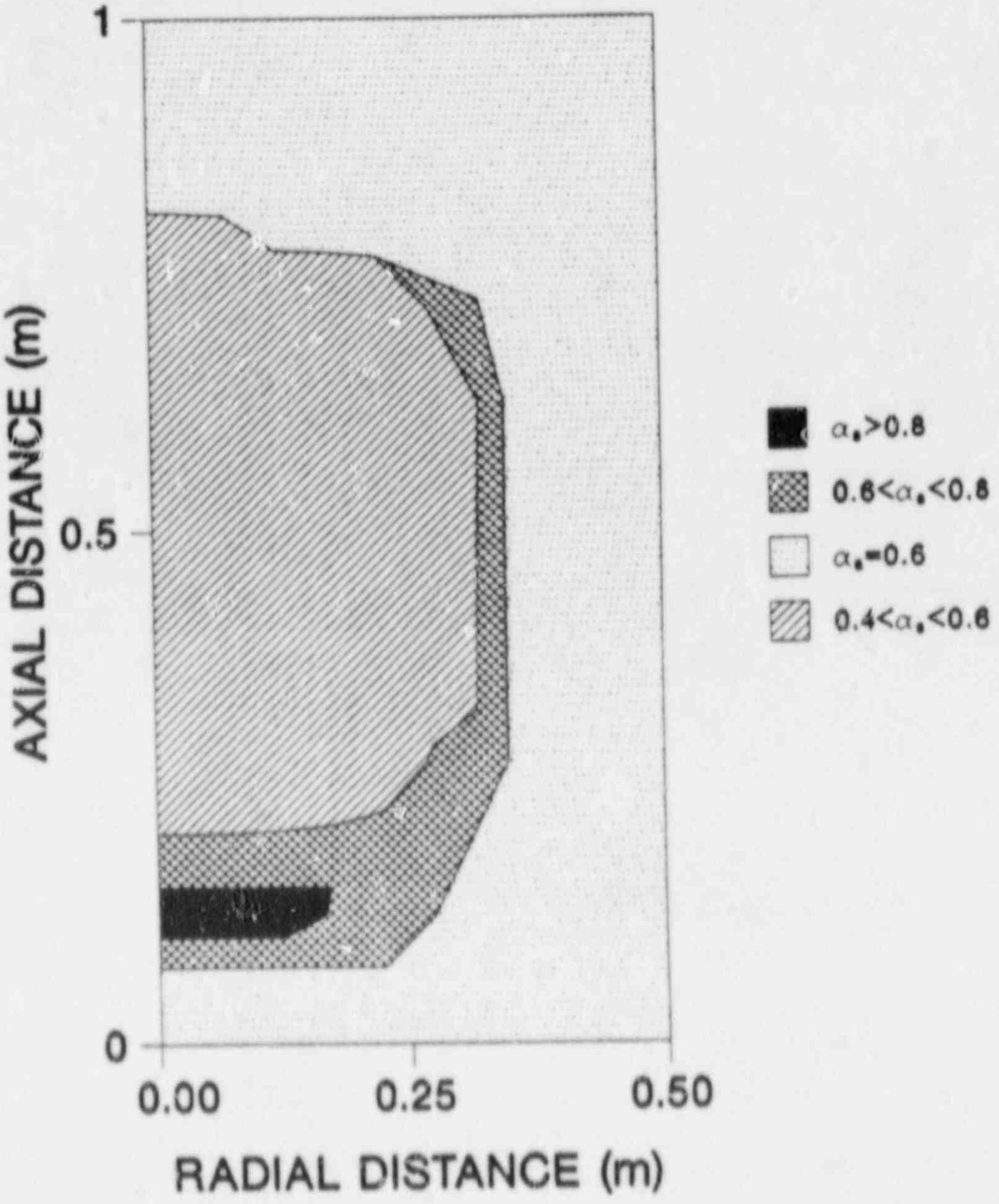

FIG. 6: Solid volume fraction α_s at t=4700 s for Case 1a.

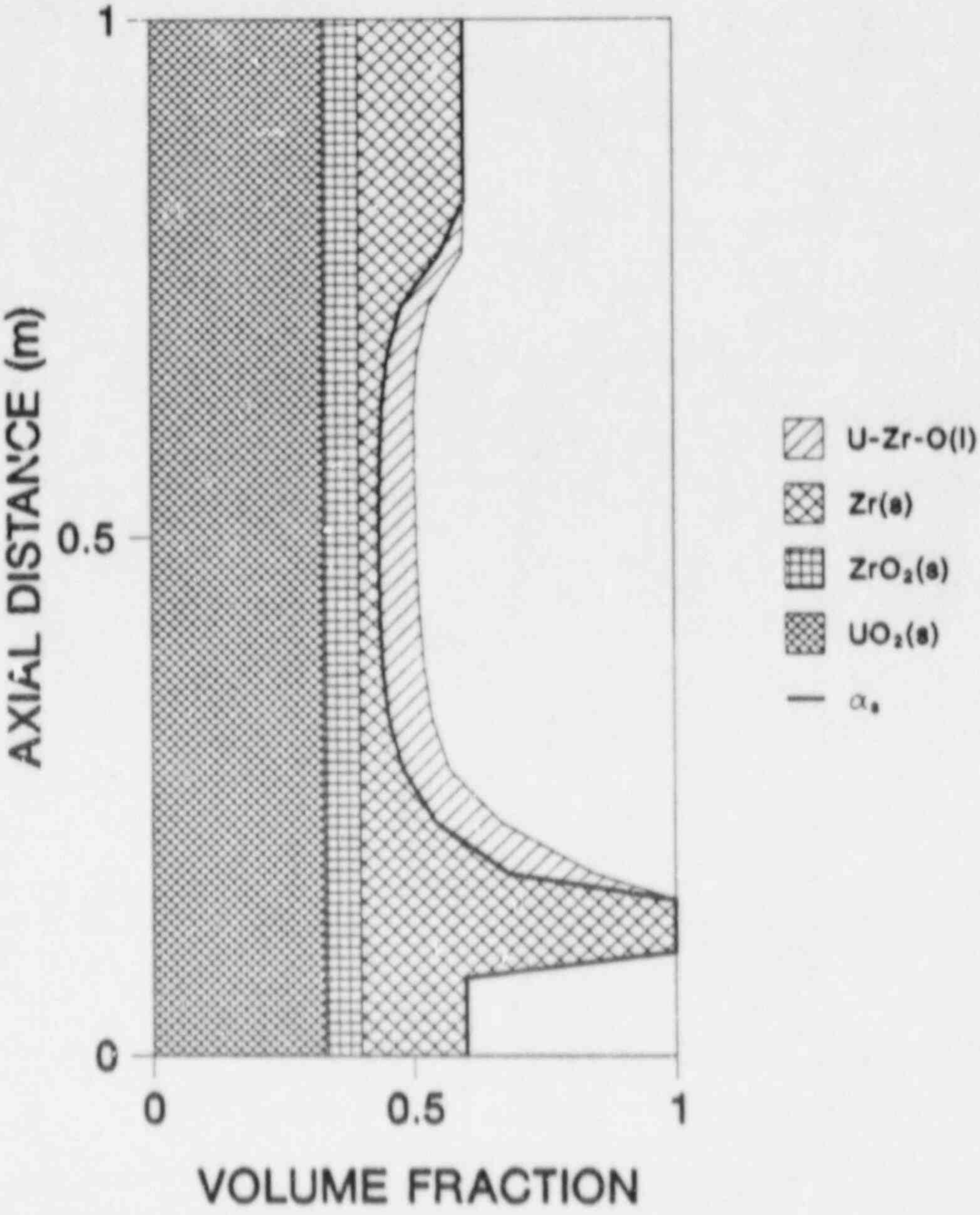

FIG. 7: Centerline species volume fractions at 4700 s for Case 1a. Also shown is the solid volume fraction α_s.

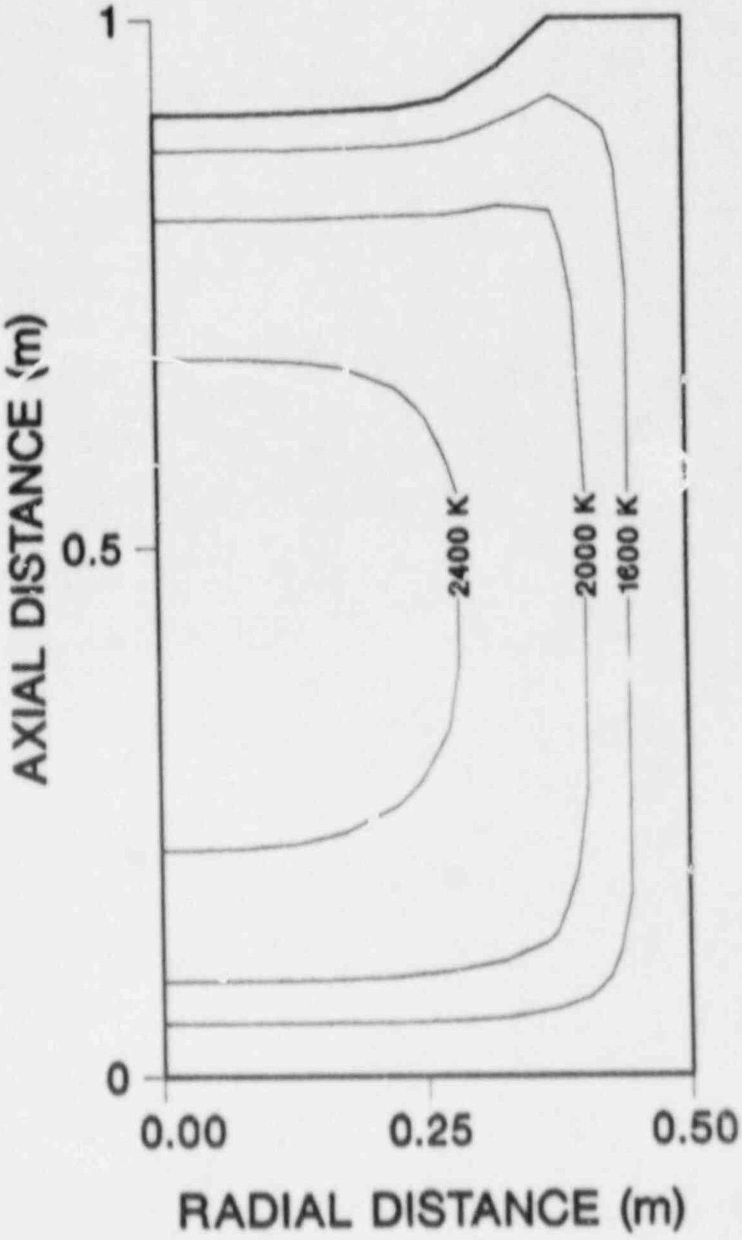

FIG. 8: Temperature contours at t=5700 s for Case 1a.

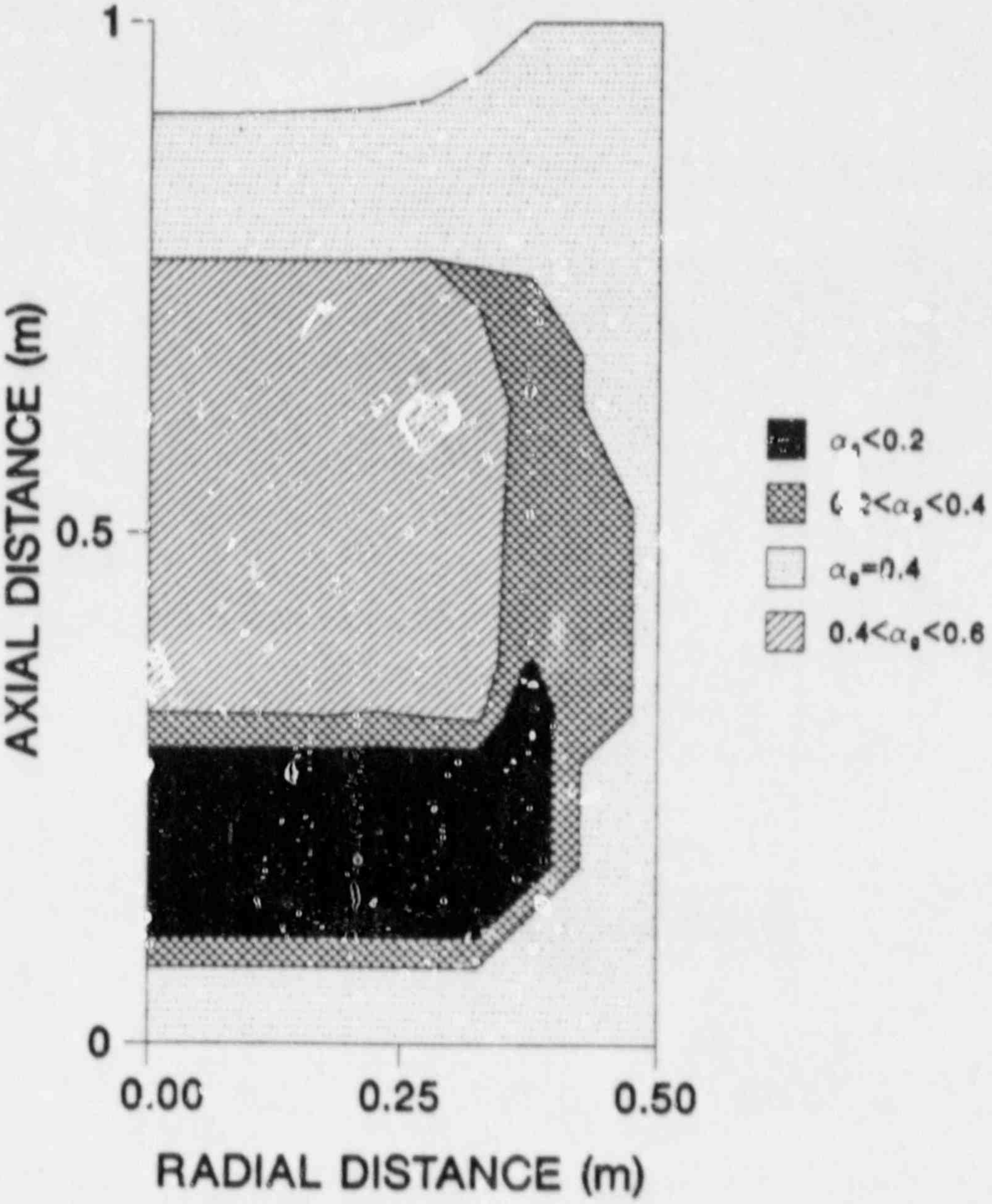

FIG. 9: Gas volume fraction α_g at t=5700 s for Case 1a.

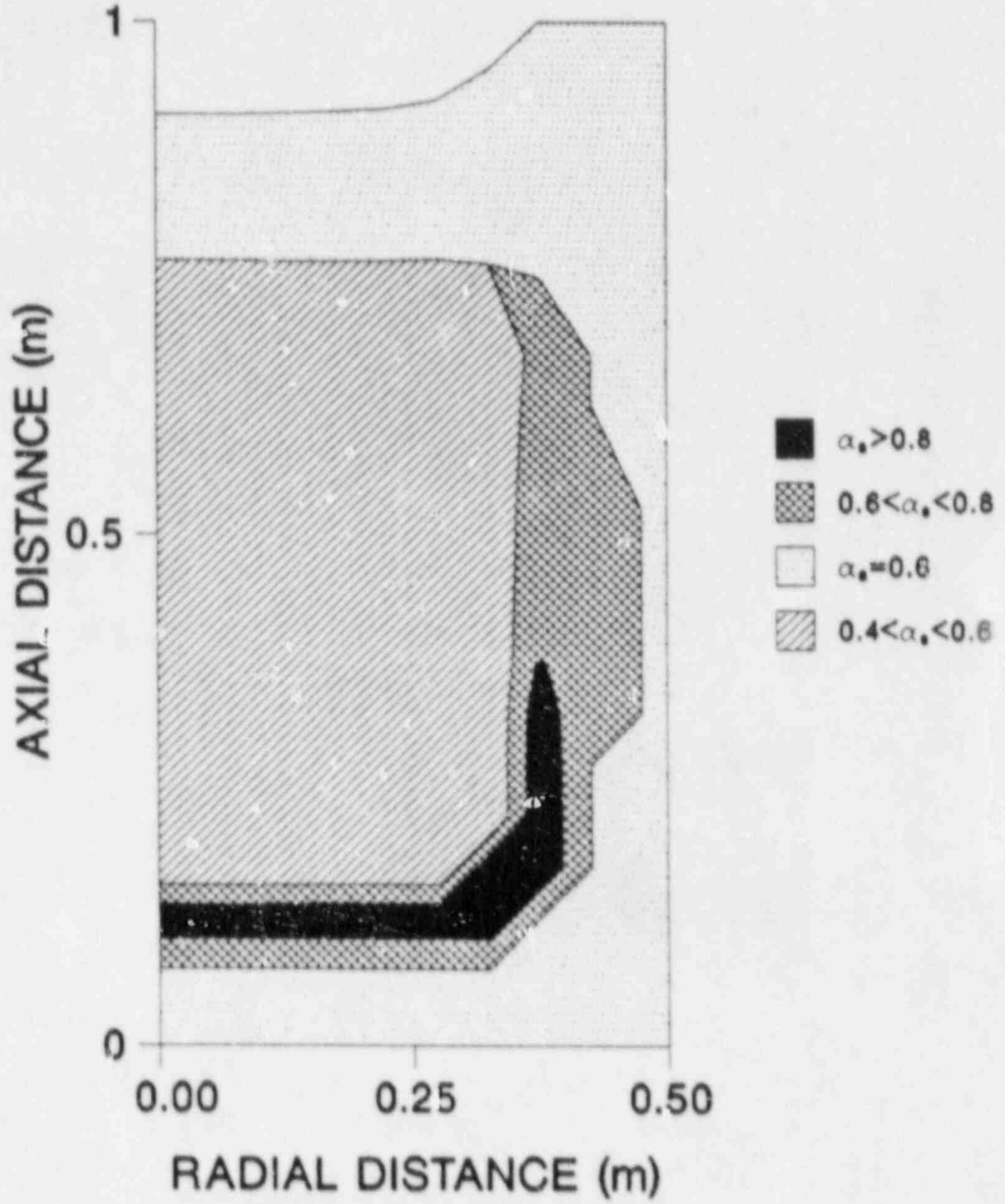

FIG. 10: Solid volume fraction α_s at t=5700 s for Case 1a.

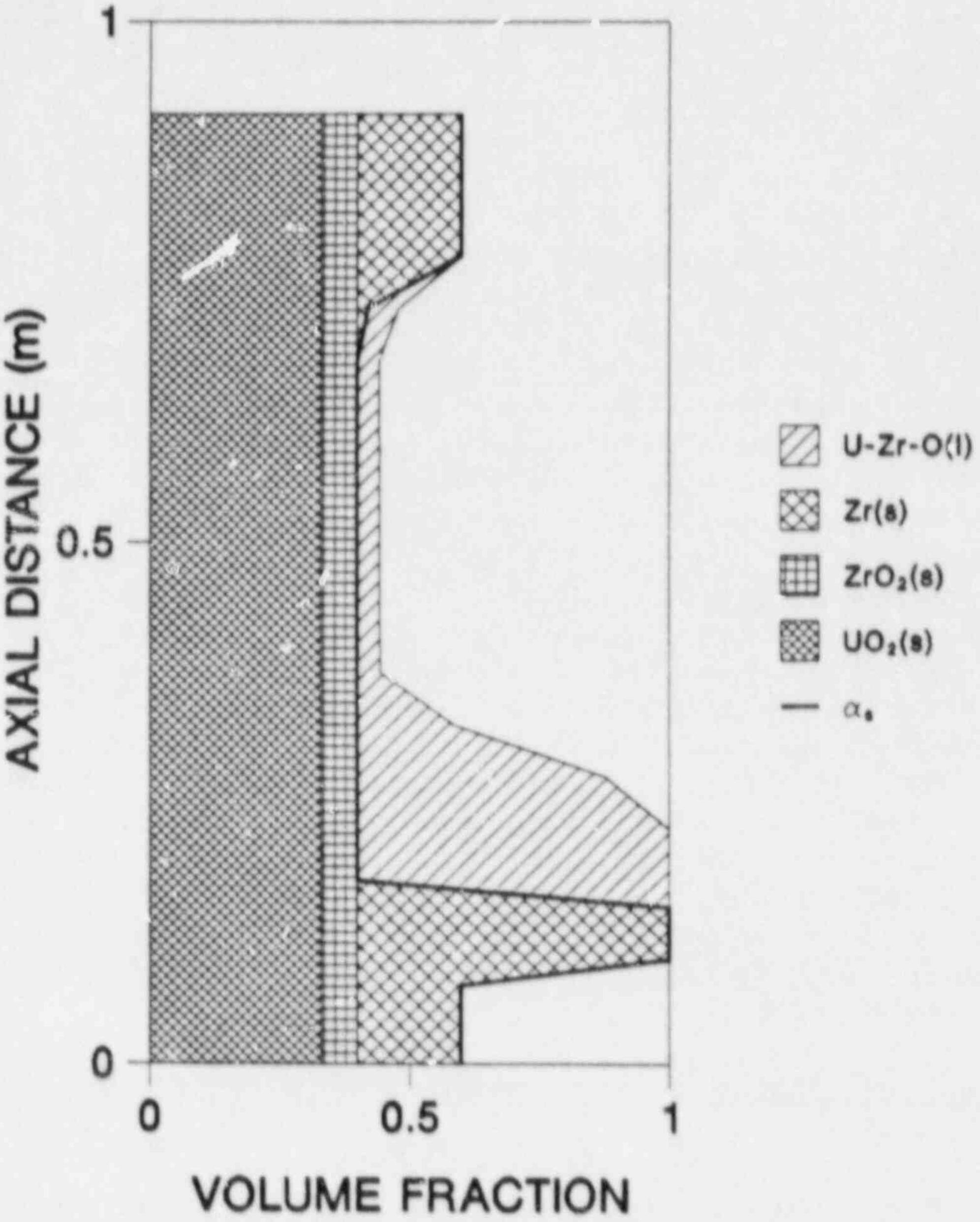

FIG. 11: Centerline species volume fractions at 5700 s for Case 1a. Also shown is the solid volume fraction α_s.

solid UO_2 and ZrO_2 initially occupy forty percent of the total volume. Therefore, the decrease in bed height near the center is directly attributable to the dissolution of UO_2 and ZrO_2.

By comparing Figs. 10 and 12 it can be shown that the temperature of the lower crust in Fig. 10 reaches the Zr melting point between 5700 s and 6000 s. When this crust melts, liquid flows downward and refreezes closer to the bottom boundary -- see Figs. 13, 14 and 15. Note that the metal to oxide ratio decreases with height above the metallic blockage. This effect has been observed in postaccident analyses of the TMI-2 core [6].

Melt composition is plotted as a function of time in Fig. 16. Zirconium starts melting at 4600 s. As temperatures in the bed increase, molten Zr dissolves both UO_2 and ZrO_2. Since this calculation was conducted for a nonoxidizing environment, all of the oxygen in the liquid solution is due to dissolution. At 6000 s, the melt composition is 64.15% Zr, 25.75% O and 10.10% U. The melt oxygen concentration is twice the melt uranium concentration when only UO_2 is dissolved. In this calculation, the ZrO_2 to UO_2 dissolution ratio (moles of ZrO_2 dissolved divided by moles of UO_2 dissolved) is 0.27. Initially (at t=0 s), the ZrO_2 to UO_2 volume ratio is 0.21, which corresponds to a ZrO_2 to UO_2 mole ratio of 0.27. Equal percentages of UO_2 and ZrO_2 are dissolved because it was assumed in Section 2.6 that dissolution is symmetric with respect to UO_2 and ZrO_2 compositions -- see Fig. 2. Experiments are needed to assess the validity of this assumption; uncertainties will affect the $UO_2(s)$ to $ZrO_2(s)$ ratio in the center of the bed.

3.1b CASE 1B: Zirconium in a Ceramic Bed with $\alpha_{s,min}=0.3$

In this section, the effect of changing $\alpha_{s,min}$ from 0.4 to 0.3 is discussed. All other parameters are kept fixed at their Section 3.1a values. Temperature, porosity, solid volume fraction and centerline species profiles at 6000 s for Case 1b are shown in Figs. 17,18,19 and 20, respectively. The melt composition and the species melt fractions are independent of $\alpha_{s,min}$. These variables depend strongly on the temperature and at 6000 s, the peak temperature is 2600 K for both values of $\alpha_{s,min}$.

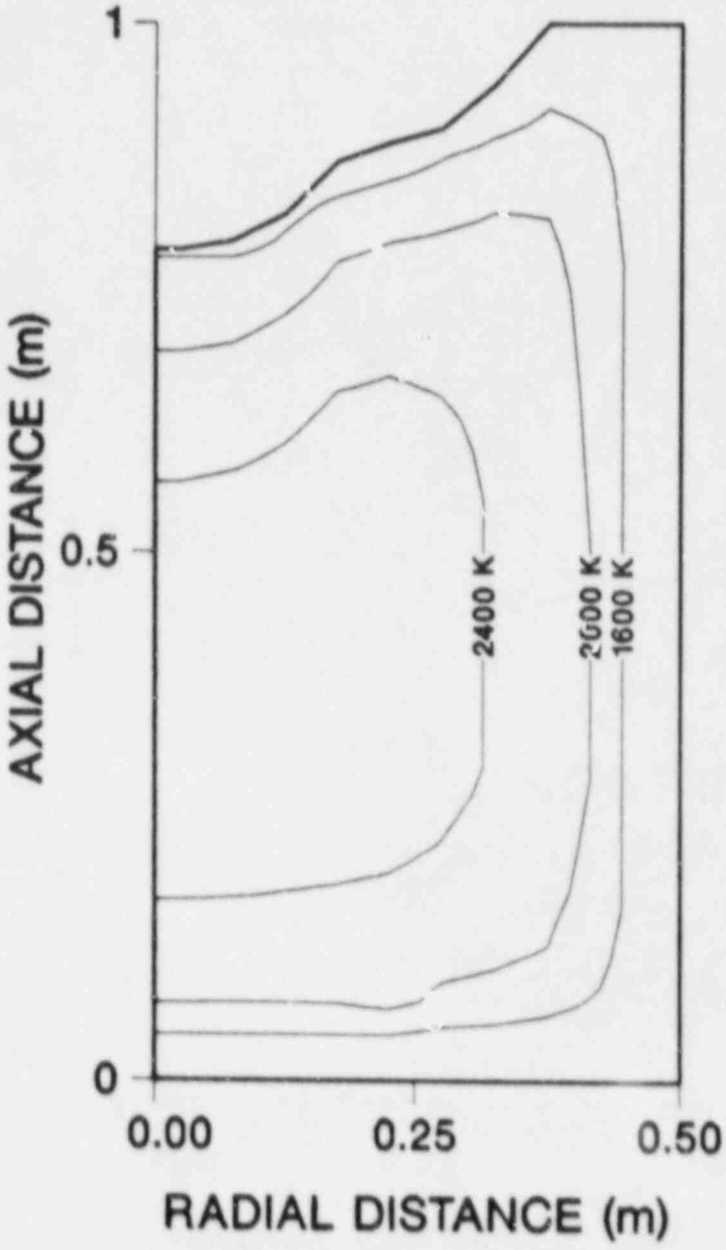

FIG. 12: Temperature contours at t=6000 s for Case 1a.

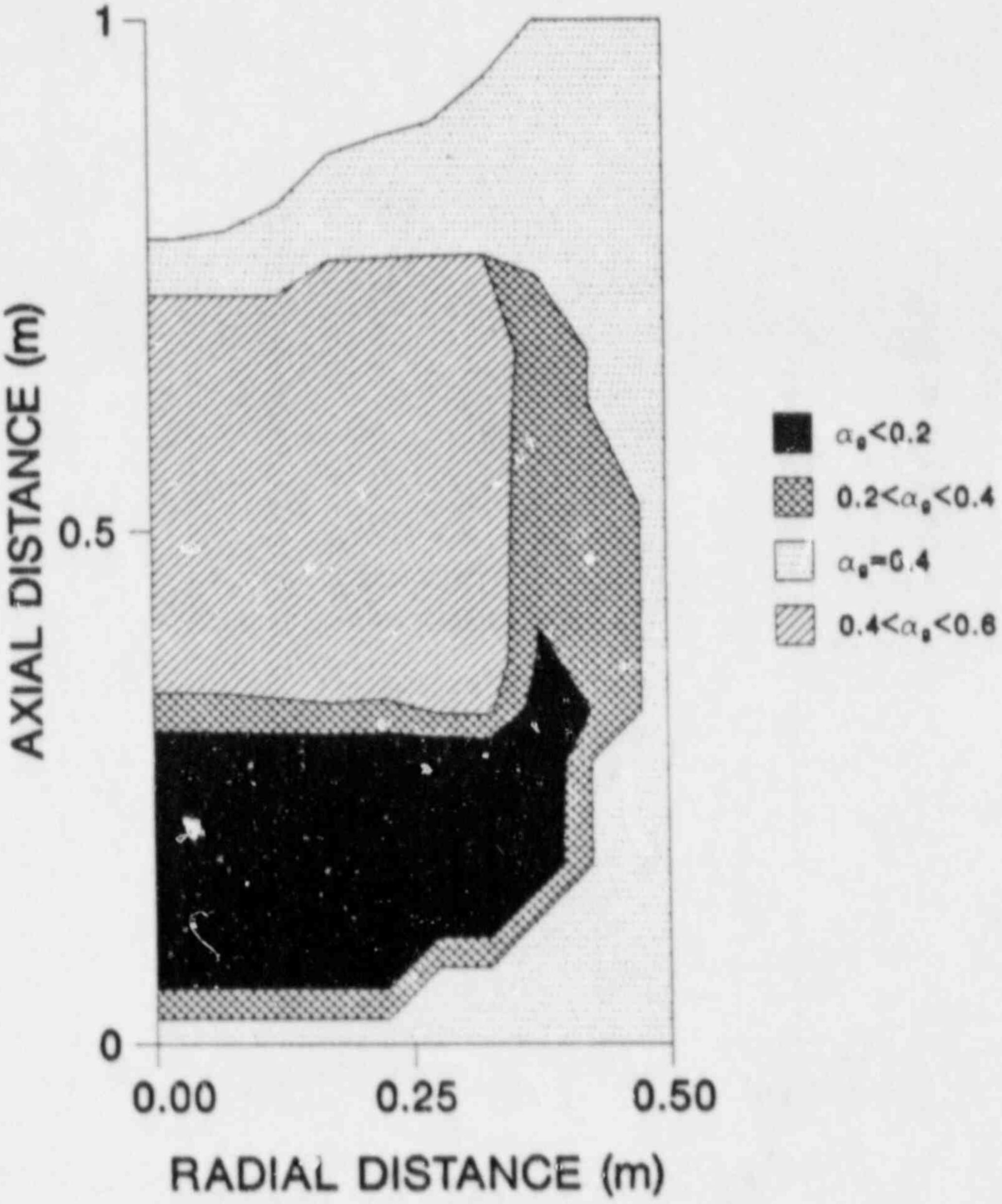

FIG. 13: Gas volume fraction α_g at t=6000 s for Case 1a.

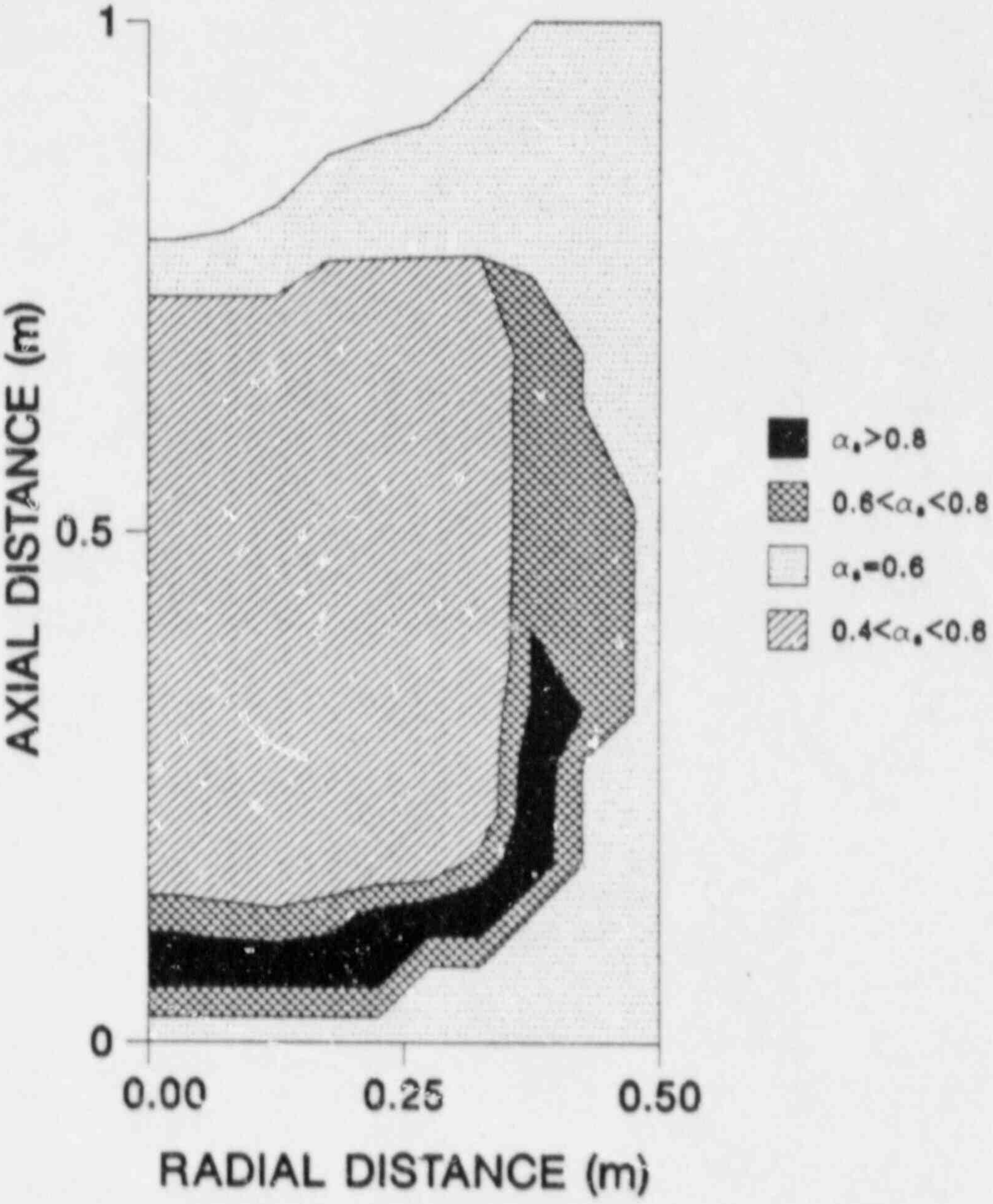

FIG. 14: Solid volume fraction α_s at t=6000 s for Case 1a.

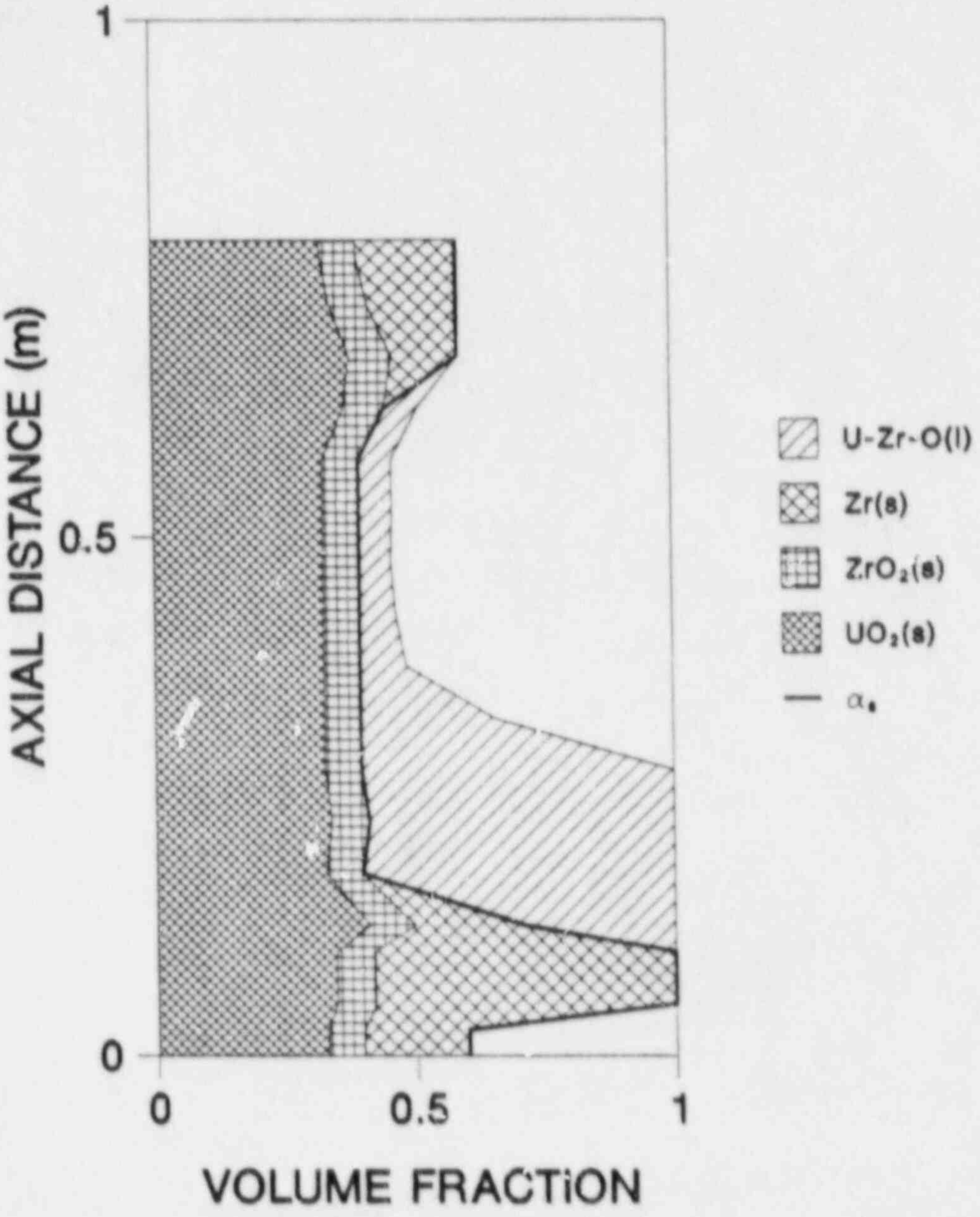

FIG. 15: Centerline species volume fractions at 6000 s for Case 1a. Also shown is the solid volume fraction α_s.

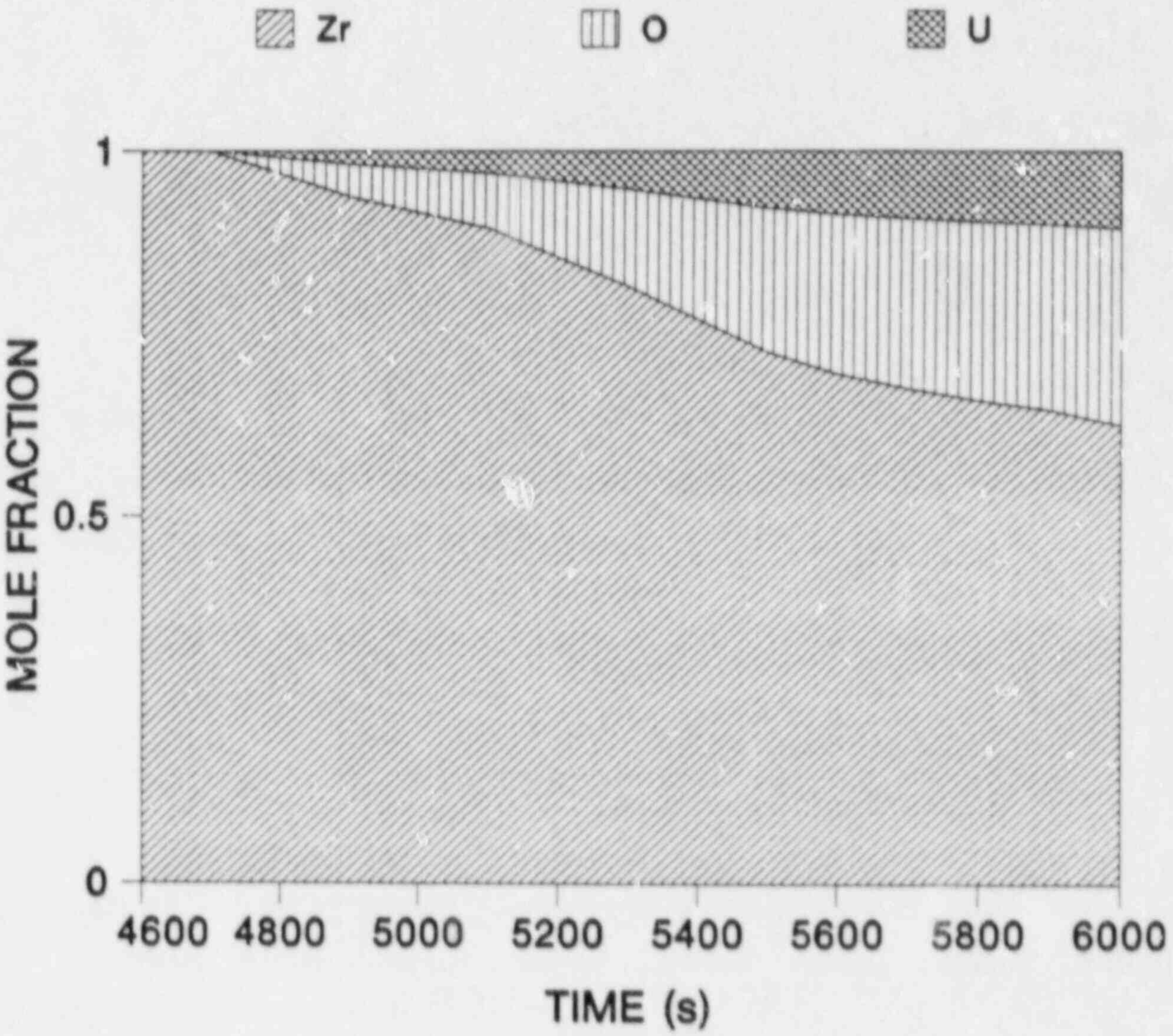

FIG. 16: Composition of the melt as a function of time for Case 1a.

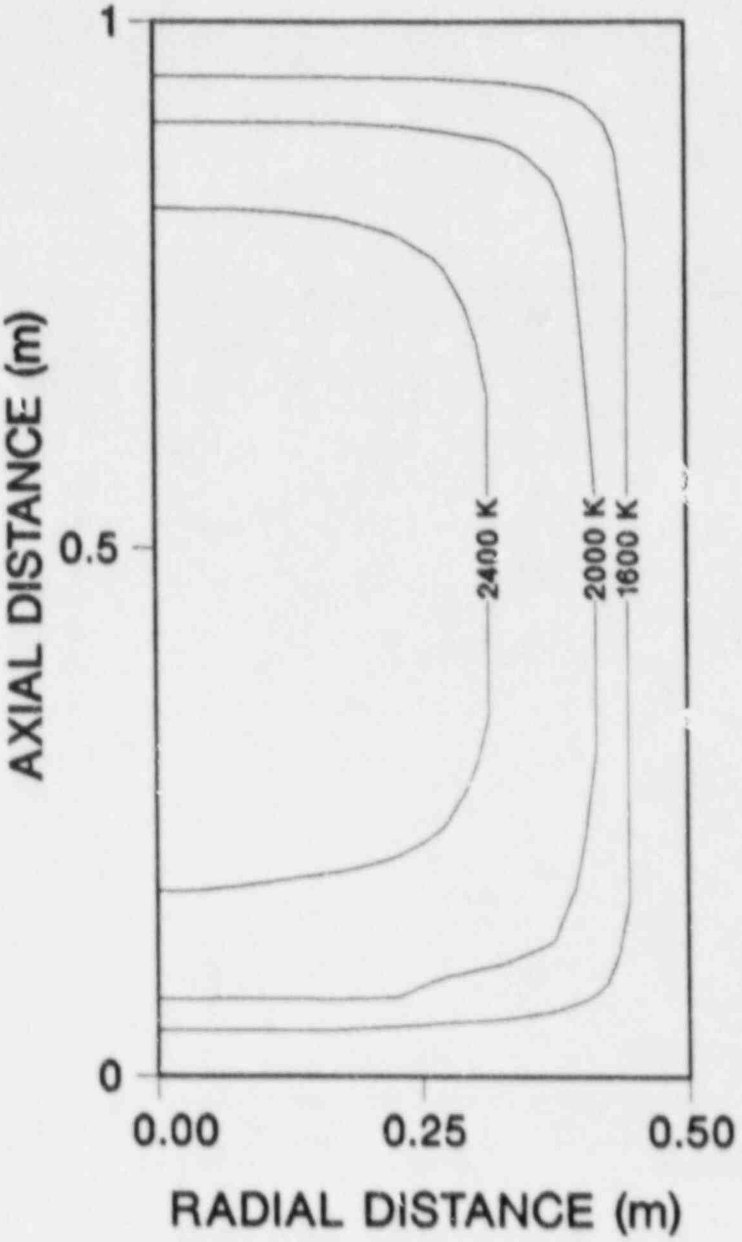

FIG. 17: Temperatu e contours at t=6000 s for Case 1b.

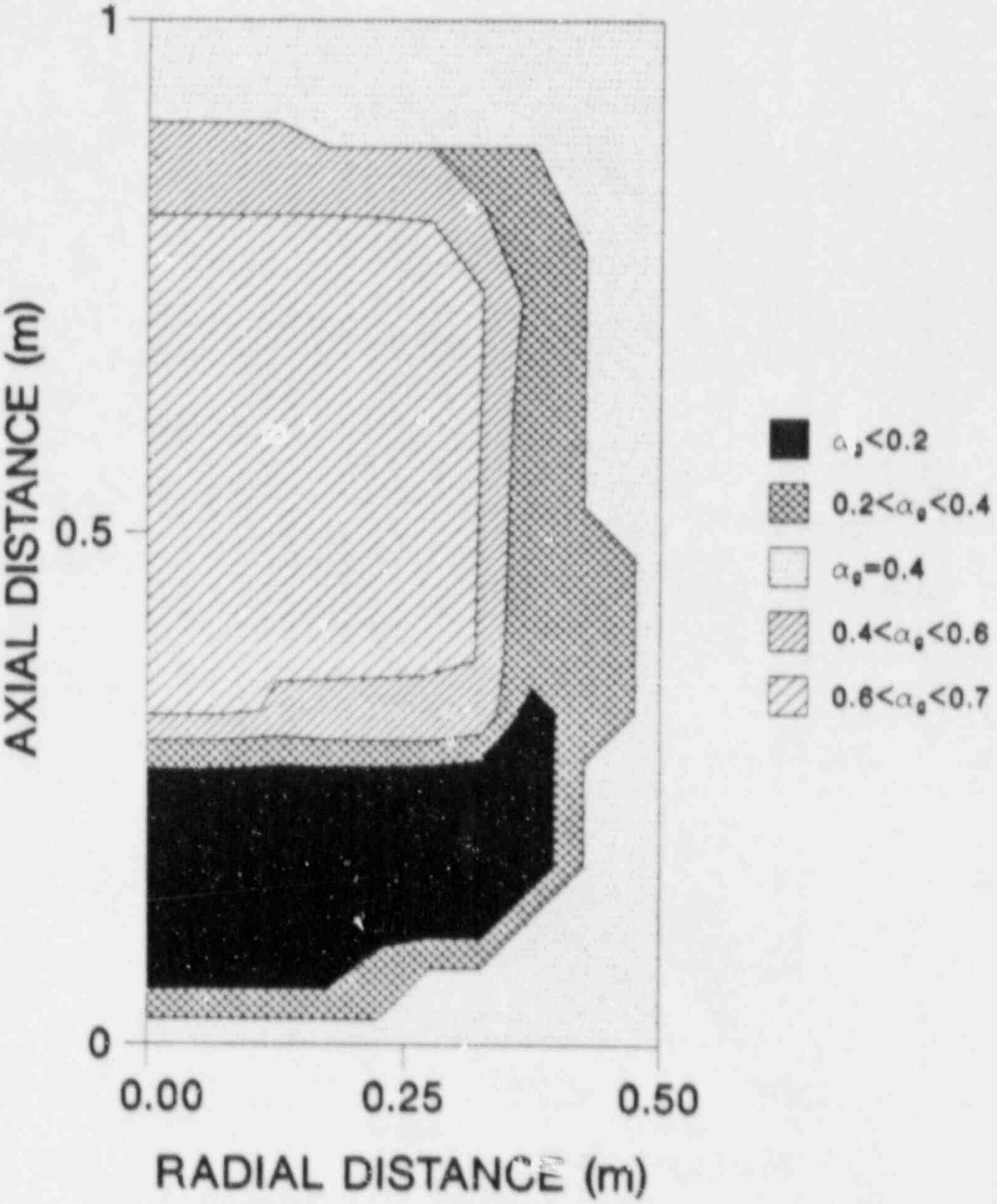

FIG. 18. Gas volume fraction α_g at t=6000 s for Case 1b.

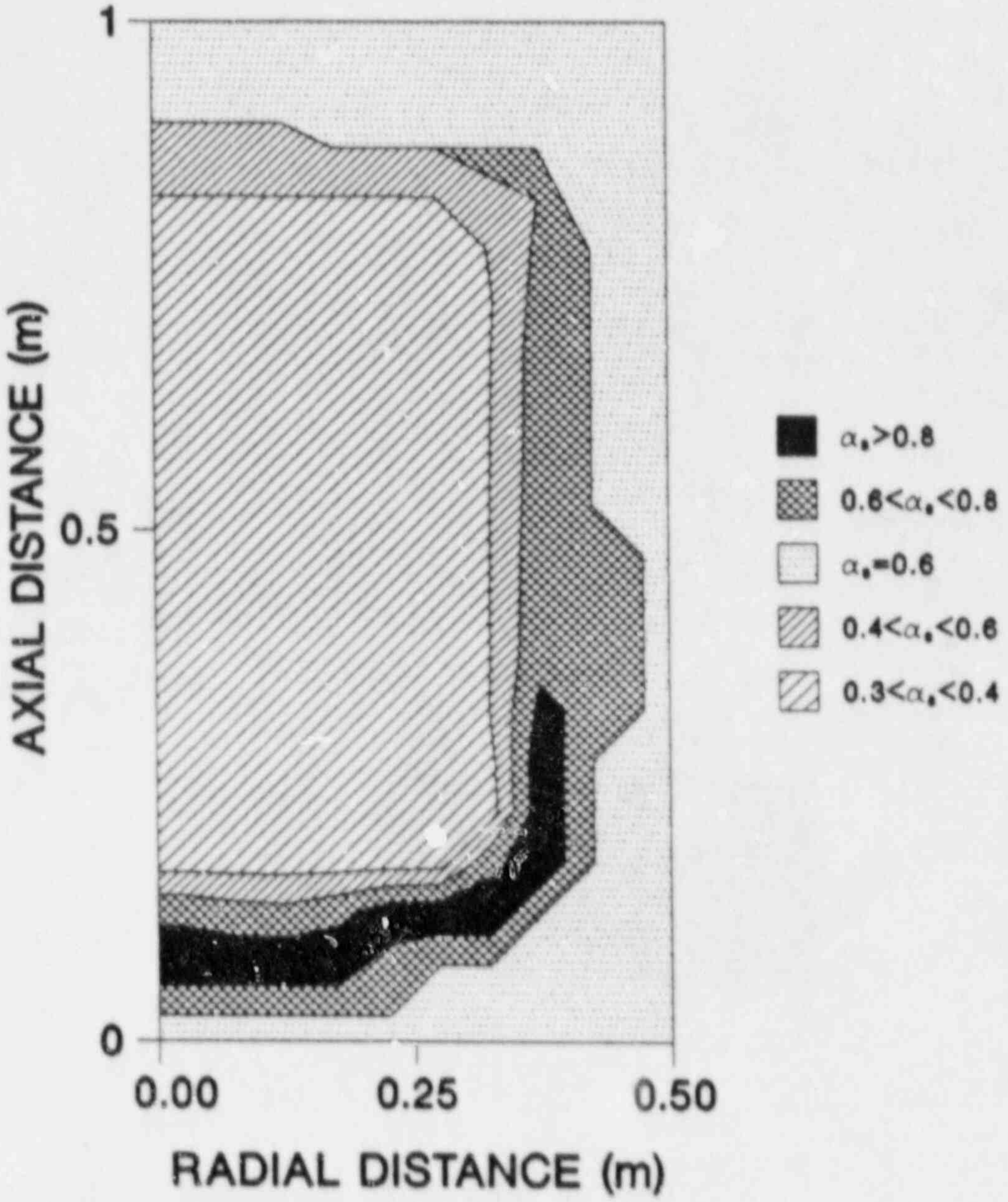

FIG. 19: Solid volume fraction α_s at t=6000 s for Case 1b.

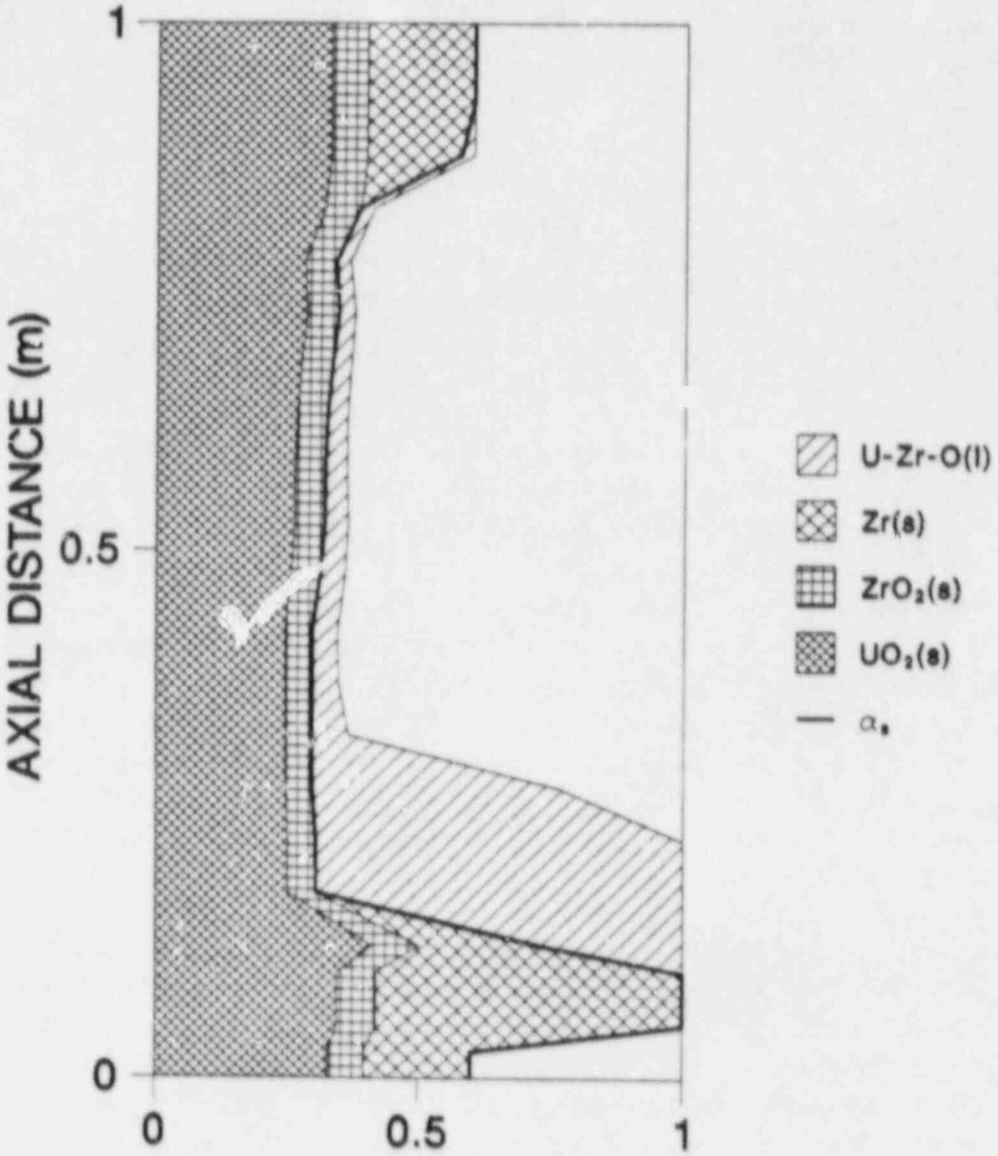

FIG. 20: Centerline species volume fractions at 6000 s for Case 1b. Also shown is the solid volume fraction α_s.

However, the configuration of the debris bed is very dependent on $\alpha_{s,min}$. At 6000 s, the bed height has decreased by as much as twenty percent for $\alpha_{s,min}=0.4$, whereas for $\alpha_{s,min}=0.3$, the bed has not started collapsing downward. Although the same amount of solid has melted for both values of $\alpha_{s,min}$, the molten pool is larger for $\alpha_{s,min}=0.4$ -- compare Figs. 13 and 18. From Figs. 15 and 20 it is evident that a larger fraction of the melt is trapped above the pool by surface tension effects for $\alpha_{s,min}=0.3$ because the bed height is greater (melt relocation ceases when the saturation falls below the residual saturation S_r and S_r is approximately the same for both cases).

3.2 Case 2: Stainless Steel in Ceramic Beds

Solutions are presented in this section for a bed with initial UO_2 and stainless steel volume fractions of 0.4 and 0.2, respectively, and an initial porosity of 0.4. Ostensen [78] noted that the contact angle θ between molten stainless steel and solid UO_2 is large. Two cases are considered in this study: (2a) $\theta=60°$ (the melt wets the solid) and (2b) $\theta=120°$ (nonwetting). Recall from Section 2.2 that capillary forces move liquid into regions of high saturation when $90°<\theta<180°$. Consequently, the equations governing melt relocation are highly unstable for a nonwetting system; small perturbations can cause melt to agglomerate in a fairly random manner. A stability analysis is presented in Appendix A.

Porosity profiles at 3700 s for Case 2a are shown in Fig. 21. The black region in Fig. 21 consists of a molten pool supported by a dense blockage -- see Fig. 22. Note that there is significant outward radial motion for $\theta=60°$; a crust with $0.4<\alpha_s<0.6$ forms near the radial boundary. Since the molten steel wets the UO_2, capillary forces move the melt into regions of low porosity. Because the solid volume fraction α_s decreases with distance from the centerline, the radial component of the liquid velocity is positive. Therefore, capillary forces move melt radially outward in this case.

Porosity profiles at 3700 s for Case 2b are shown in Fig. 23. In a nonwetting system, capillary forces move liquid into regions of high porosity and the radial component of the liquid velocity

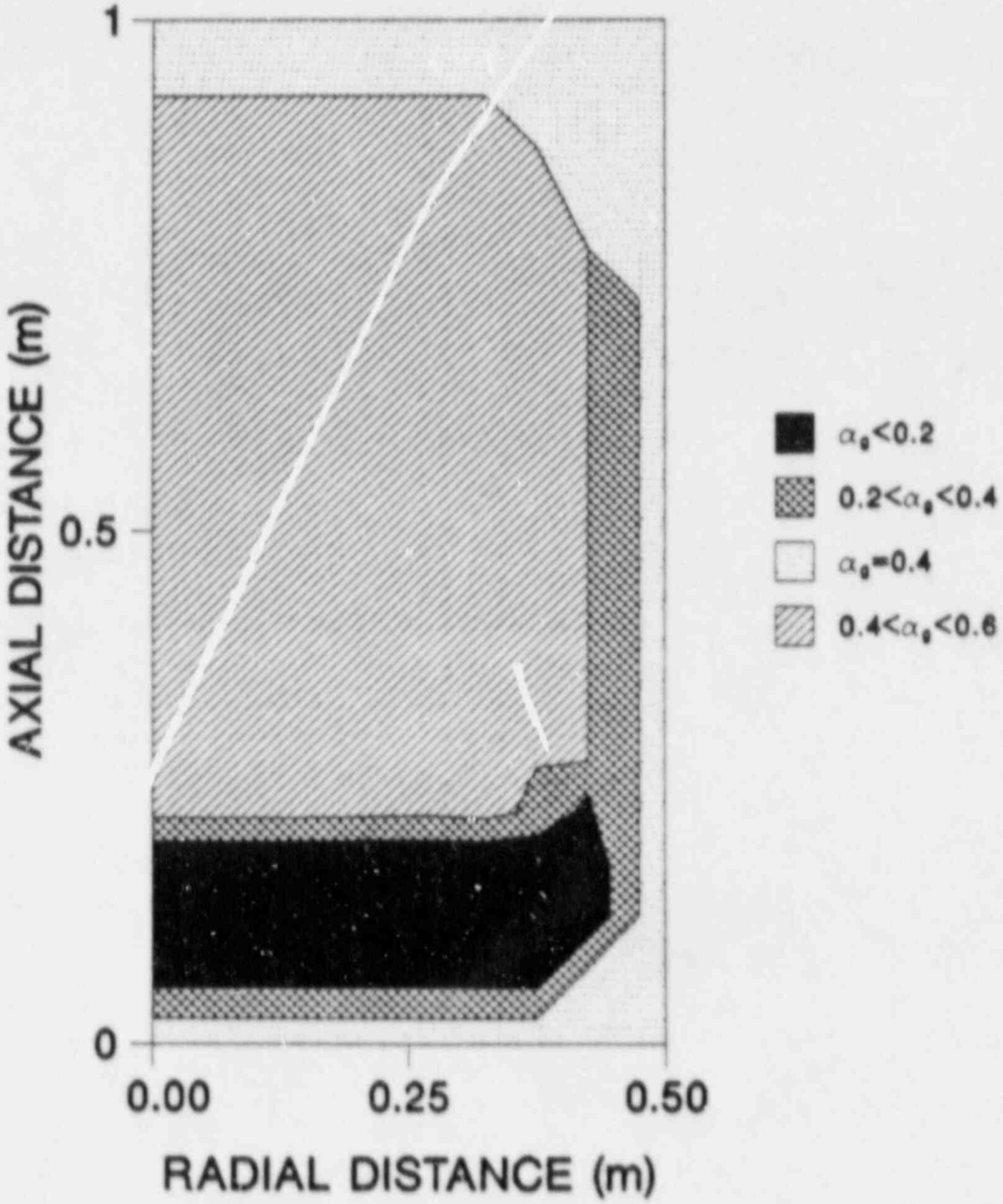

FIG. 21: Gas volume fraction α_g at t=3700 s for Case 2a $(\theta=60)$.

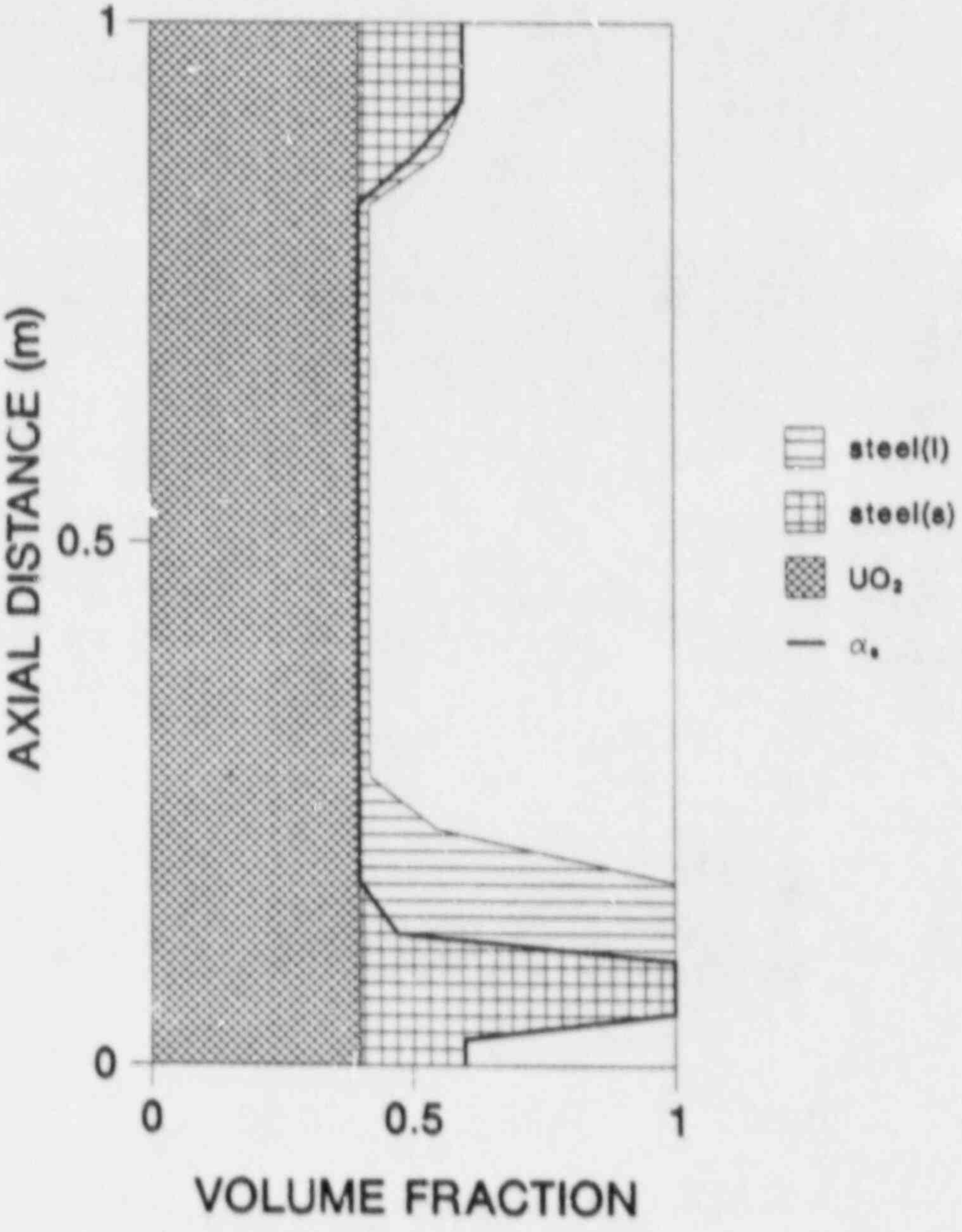

FIG. 22: Centerline species volume fractions at 3700 s for Case 2a (θ=60). Also shown is the solid volume fraction α_s

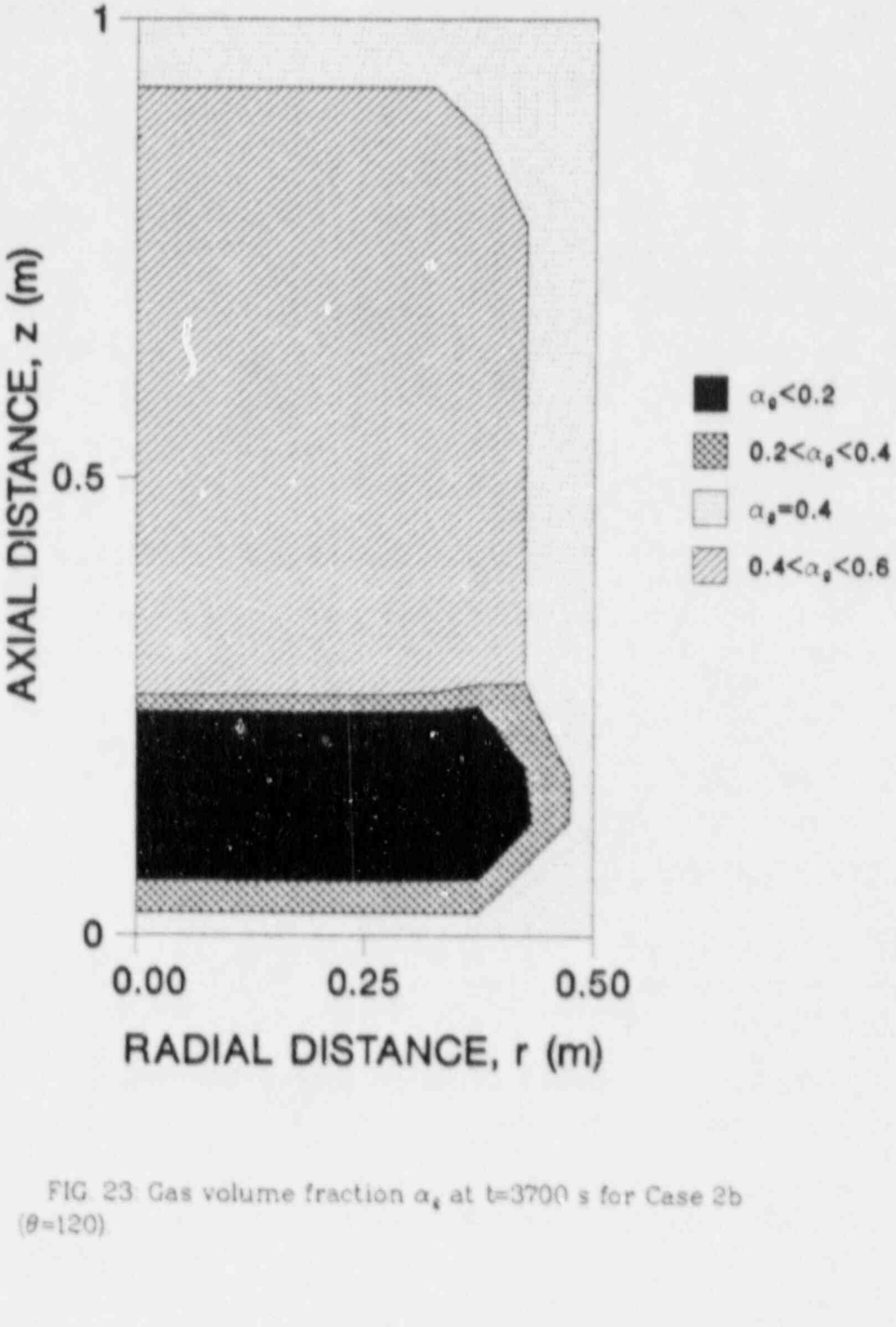

FIG. 23 Gas volume fraction α_g at t=3700 s for Case 2b (θ=120)

is negative. Therefore, capillary forces move melt toward the center of the bed. In this case, all of the melt flows into the bottom of the bed. The final molten pool state is not affected by the unstable nature of the governing equations. However, melt tends to flow downward into the pool in streaks.

At t=3700 s, approximately the same amount of steel (41% of the total by weight) has melted for both values of θ. Less melt has refrozen for θ=120° and consequently, the liquid level is higher in Fig. 23 than in Fig. 21. Changing the contact angle can, therefore, significantly alter the configuration of the debris bed.

3.3a Zirconium and Iron in Ceramic Beds I: Zr to Fe Atom Ratios Greater than 3.17

In Section 2.6 it was noted that solid begins melting at a very low temperature (1200 K) for Zr to Fe atom ratios greater than 0.5. When the temperature reaches 1200 K, a eutectic reaction forms a Fe-Zr liquid solution with a Zr atomic fraction of 0.76. The effect of this reaction on melt progression is discussed in the following two sections. In this section solutions are presented for a bed with a Zr to Fe atom ratio greater than 3.17 (Case 3a) and in Section 3.3b a bed with a Zr to Fe atom ratio between 0.5 and 3.17 is considered (Case 3b). In these calculations it is assumed that the porous bed is self-supporting until the solid fraction falls below 0.3 (that is, $\alpha_{s,min}$=0.3).

A demonstration calculation was conducted for a porous bed with initially uniform UO_2, ZrO_2, Zr and Fe volume fractions of 0.33, 0.05, 0.2 and 0.02, and an initially uniform porosity of 0.4 -- see Fig. 24. For this calculation the Zr to Fe atom ratio is 4.6, which corresponds to a Zr metal atom fraction of 0.82. Centerline species volume fractions at 1800 s are shown in Fig. 25. Temperatures in the bed reach 1200 K at 1500 s. Solid starts melting at this time, decreasing the solid fraction in the center of the bed by as much as twenty-five percent. Melt flows downward under the action of gravity and because of the low solidification temperature of this Zr-Fe solution, only a small fraction freezes near the bottom of the bed. Most of the melt flows directly out of the bed.

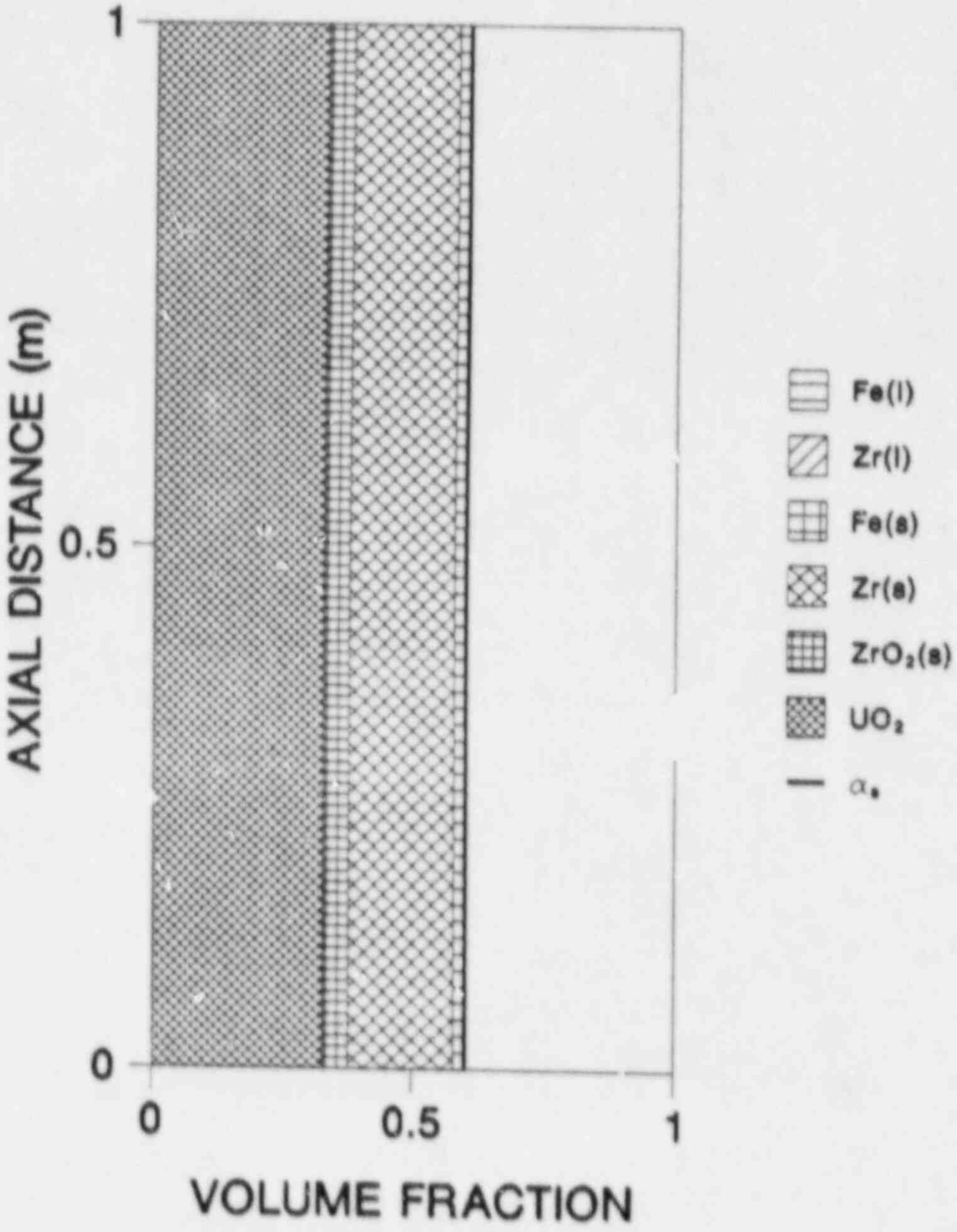

FIG. 24: Initial species volume fractions for Case 3a.

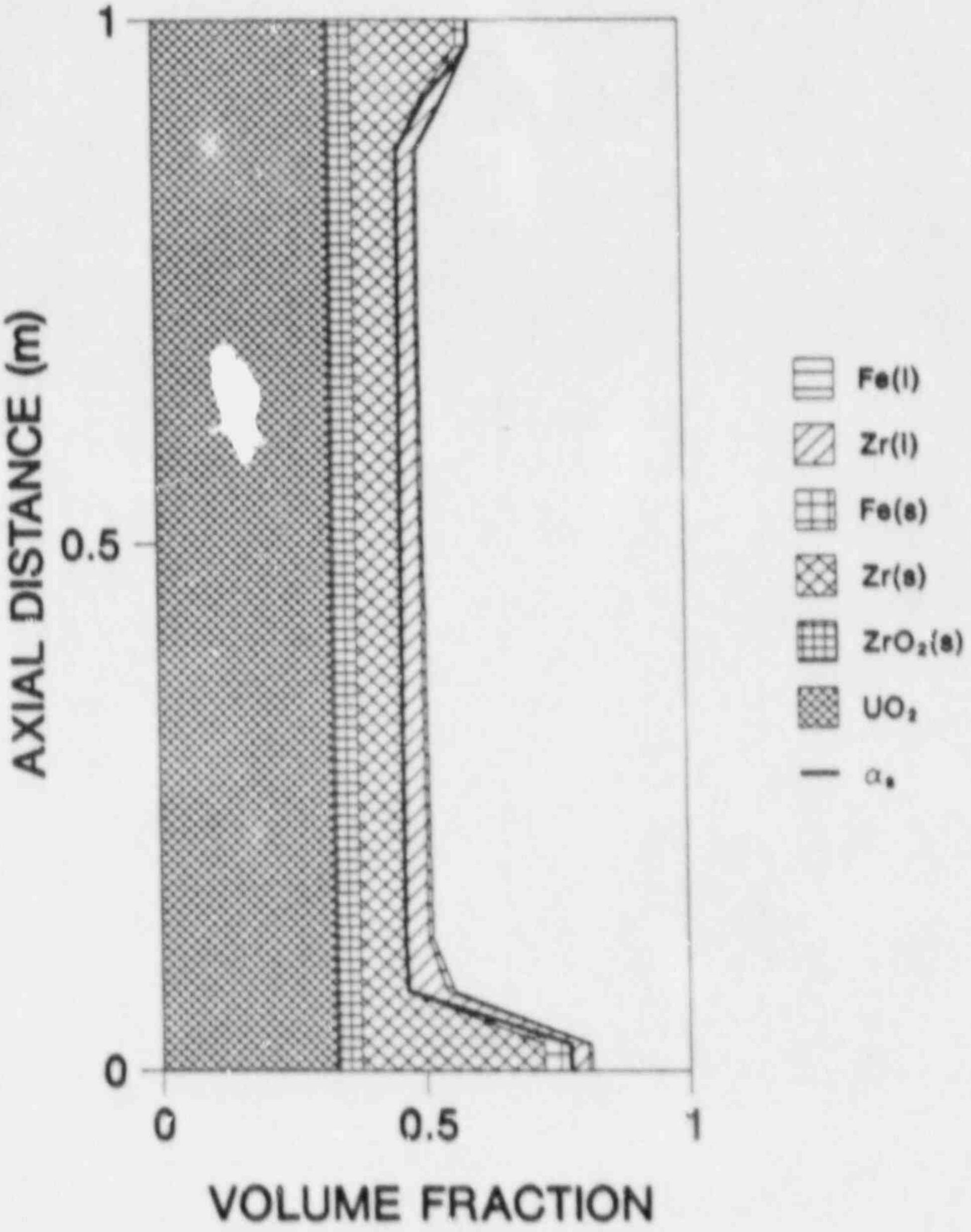

FIG. 25: Centerline species volume fractions at 1800 s for Case 3a. Also shown is the solid volume fraction α_s.

Shown in Fig. 26 are the masses of the metals in the bed as functions of time. As mentioned previously, the Zr-Fe melt composition is 76 atom percent Zr. The ratio of Zr to Fe molecular weights is 1.6 and consequently, the Zr to Fe mass ratio in the melt is 5.2. Therefore, 5 kg of Zr flow out of the bed for every kg of Fe. At 2500 s, two-thirds of the Fe and one-third of the Zr has flowed out of the bed.

For Zr metal atom fractions greater than 0.76, the eutectic reaction increases the local Zr metal fraction in the solid phase to 1.0. This reaction ceases when all of the Fe has liquefied and flowed downward. Height-averaged metal volume fractions at 2500 s are plotted as functions of radial position in Fig. 27. Note that at this time only a small amount of Fe remains in the bed. All of the Fe in the region $0\ \mathrm{m} < r < 0.4\ \mathrm{m}$ has been depleted and the Zr volume fraction in this zone has fallen below 0.1. Subsequent melt progression behavior is similar to that discussed in Sections 3.1a and 3.1b for UO_2-ZrO_2-Zr beds.

3.3b Zirconium and Iron in Ceramic Beds II: Zr to Fe Atom Ratios Between 0.5 and 3.17

Solutions are presented in this section for a porous bed with initially uniform UO_2, ZrO_2, Zr and Fe volume fractions of 0.33, 0.003, 0.2 and 0.067, and an initially uniform porosity of 0.4 -- see Fig. 28. For this calculation the Zr to Fe atom ratio is 1.85, which corresponds to a Zr metal atom fraction of 0.65. Centerline species volume fractions at 1800 s are shown in Fig. 29. Solid starts melting at 1500 s and the porosity in the center of the bed increases to 0.63 by t=1800 s. Melt having a Zr atom fraction of 0.76 flows out of the bed as happened in the calculation discussed in Section 3.1a.

Shown in Fig. 30 are the masses of the metals in the bed as functions of time. Thirty-two percent of the Fe and fifty-five percent of the Zr flows out of the bed by 2500 s. Because the melt is Zr-rich, the Zr to Fe mass ratio in the bed falls from its initial value of 3.0 to 2.0 before 2500 s elapse.

For Zr metal atom fractions between 0.33 and 0.76, the eutectic reaction forms a $ZrFe_2$ solid compound, decreasing the local Zr metal fraction in the solid phase to 0.33. Height-

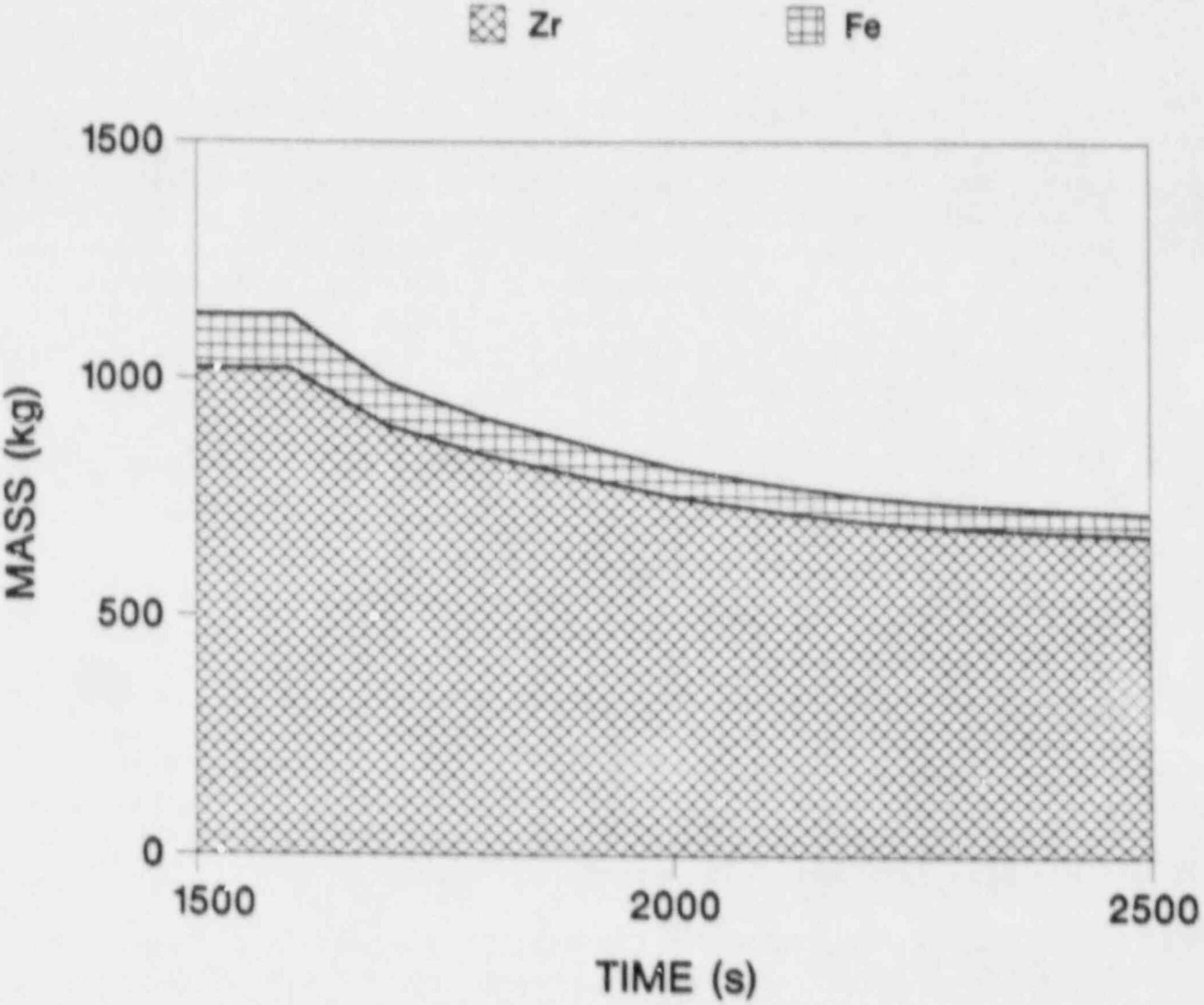

FIG. 26: Mass of the metals in the bed as a function of time for Case 3a.

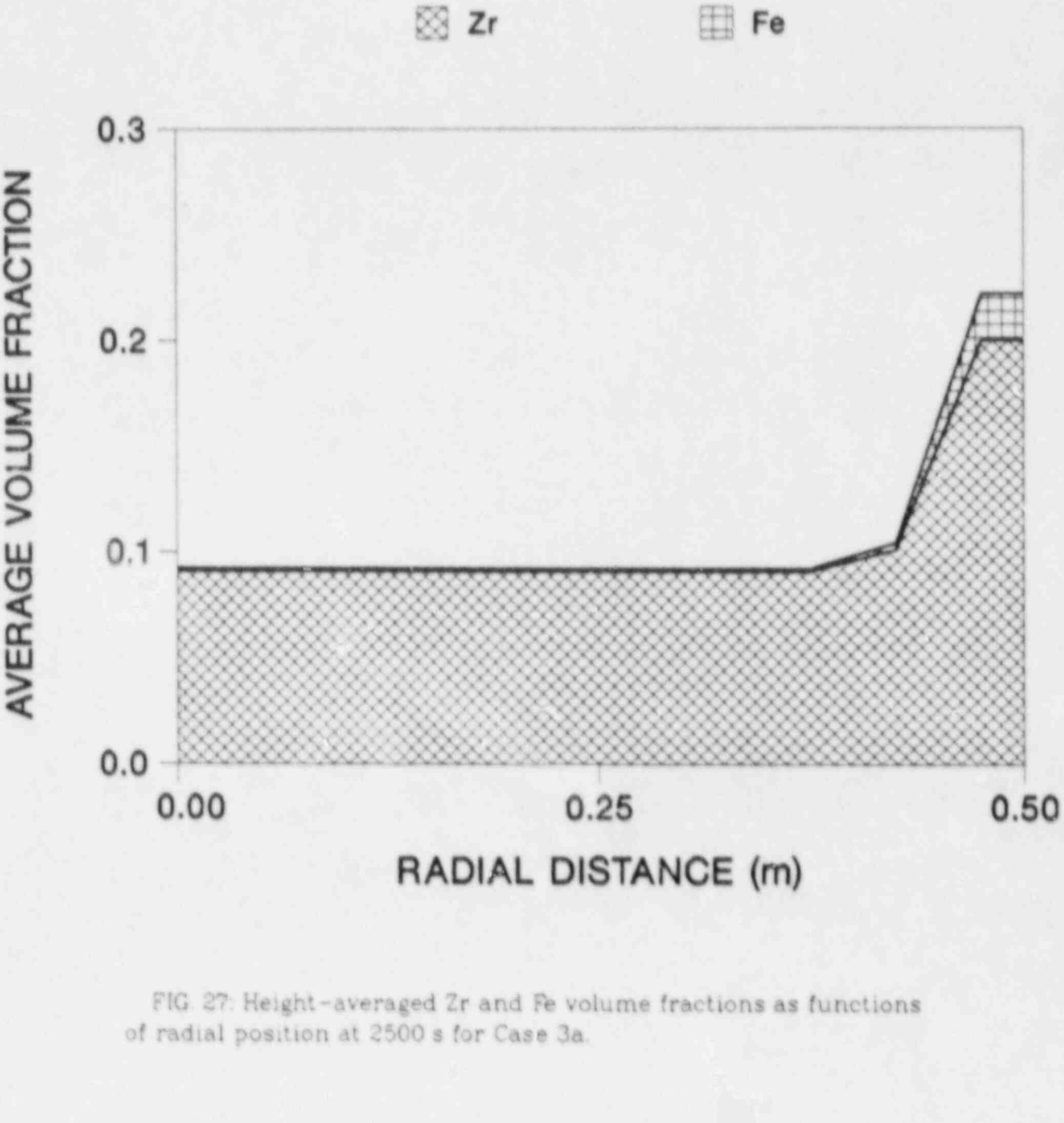

FIG. 27: Height-averaged Zr and Fe volume fractions as functions of radial position at 2500 s for Case 3a.

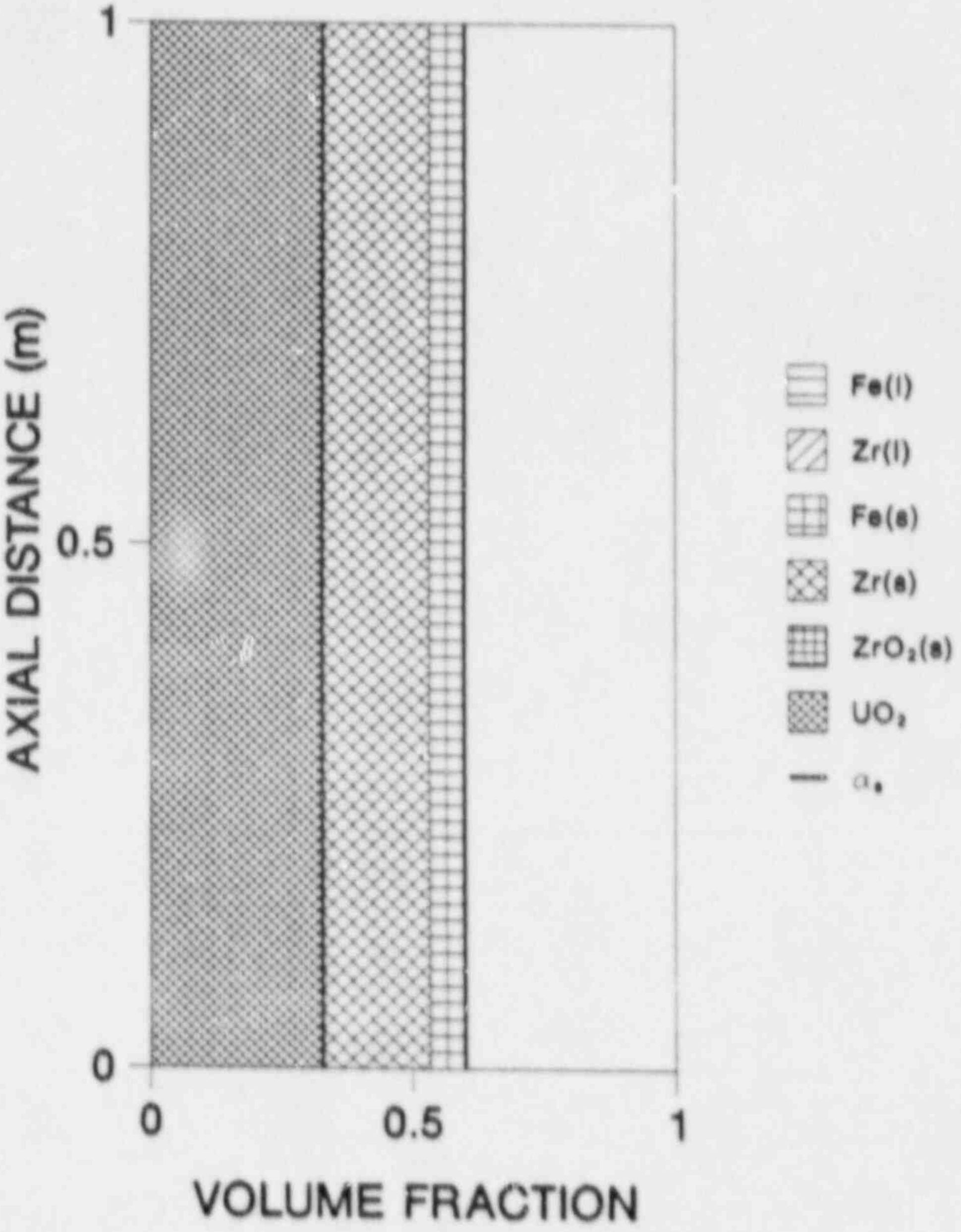

FIG. 28: Initial species volume fractions for Case 3b.

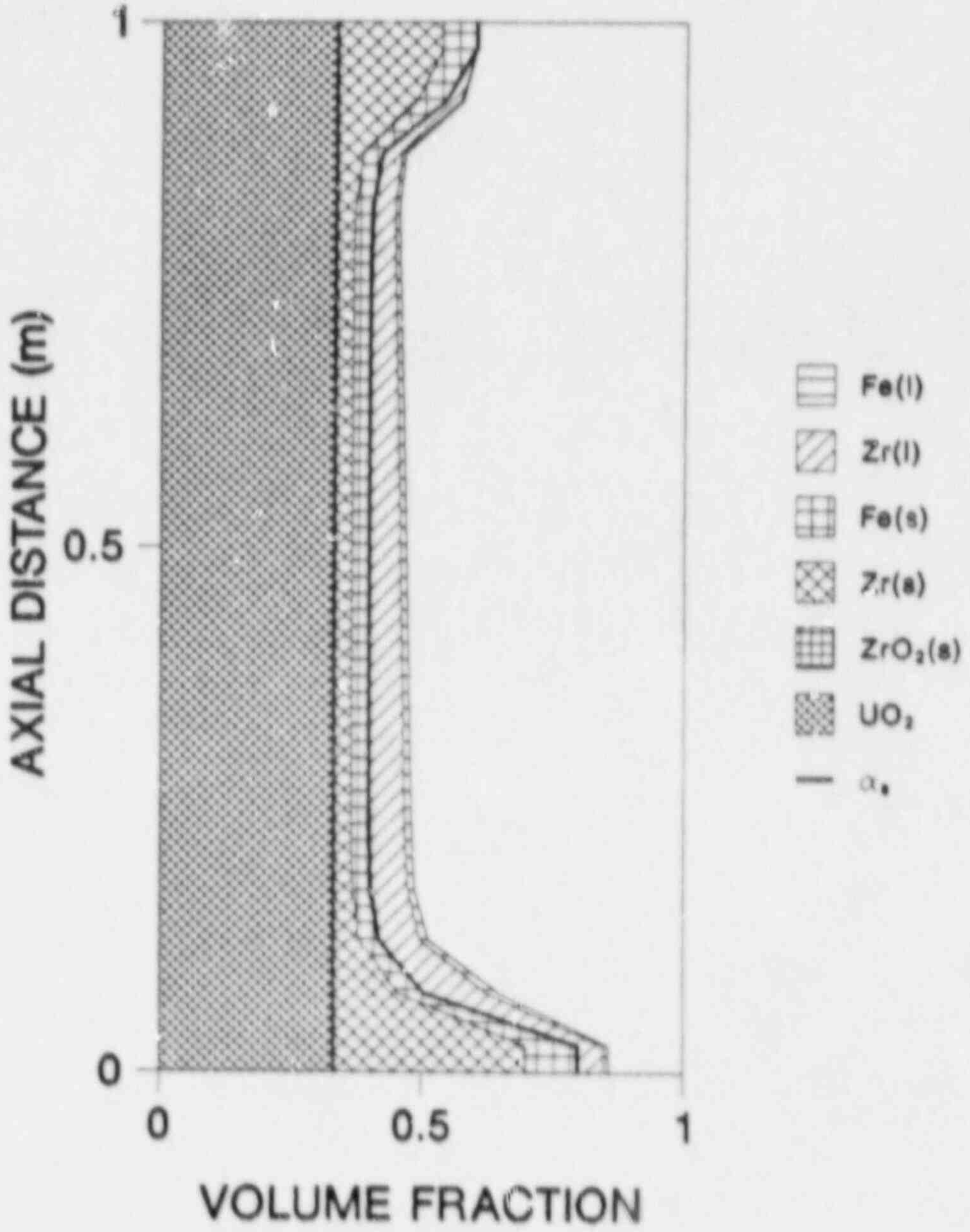

FIG. 29: Centerline species volume fractions at 1800 s for Case 3b. Also shown is the solid volume fraction α_s.

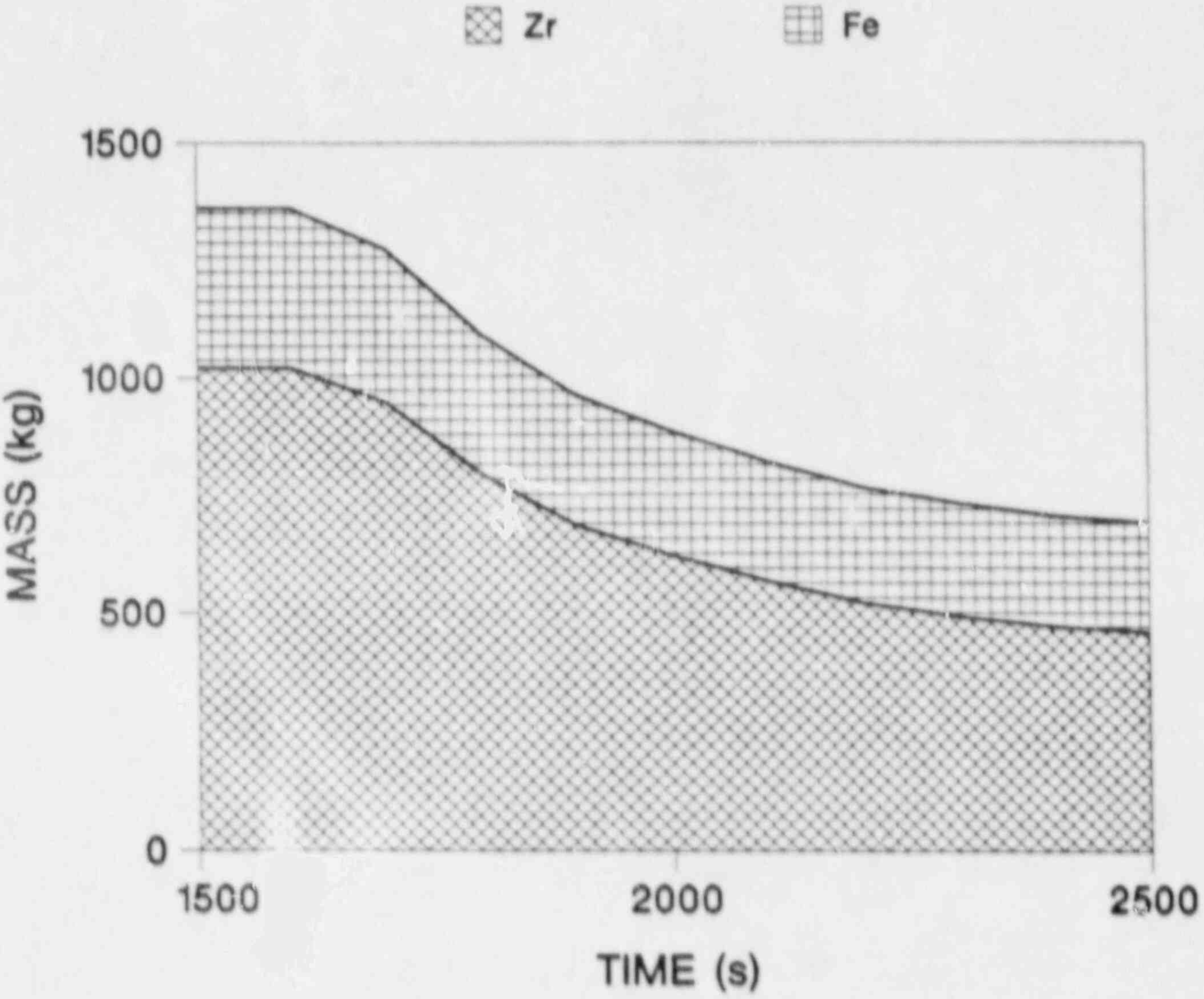

FIG. 30. Mass of the metals in the bed as a function of time for Case 3b.

averaged metal volume fractions at 2500 s are plotted as functions of radial position in Fig. 31. Significant amounts of Fe and Zr have flowed out of the 0 m<r<0.4 m region, leaving behind a mixture of UO_2, ZrO_2 and $ZrFe_2$. When the temperature reaches 1600 K, the $ZrFe_2$ will melt (see Fig.1), flow downward and form a blockage similar to those shown in Sections 3.1a, 3.1b and 3.2.

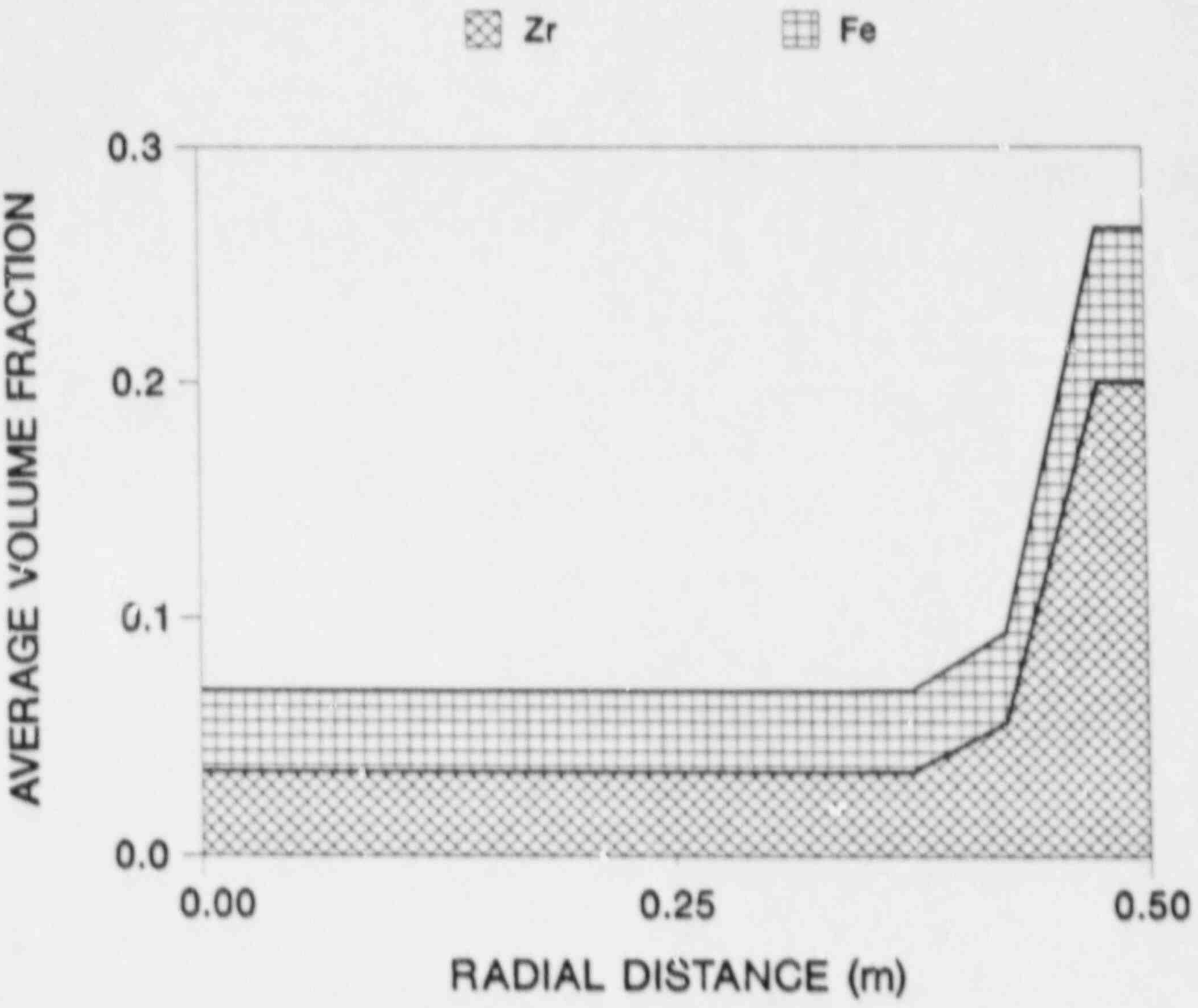

FIG. 31: Height-averaged Zr and Fe volume fractions as functions of radial position for Case 3b.

4. MAJOR UNCERTAINTIES AND EXPERIMENTS

Major uncert[illegible] in this study involve (1) the chemical interactions d[illegible] in Section 2.6; (2) bed collapse; and (3) flow correlati[illegible]s those given in Eqs. (3-6). Such uncertainties [illegible]esolved in order to accurately predict oxidation and [illegible] product transport in severely damaged reactor cores and [illegible] manner in which debris is released into the lower plenum. A discussion of these uncertainties and priorities follows.

A U-Zr-O phase diagram is needed. Especially important is the accurate determination of heats of fusion and dissolution energies. Information regarding Fe-Zr-U-O interactions would also be helpful. Experiments are needed to assess the equilibrium assumptions in Sections 2.5 and 2.6; we anticipate that the Melt Progression (MP) experiments currently being planned at Sandia will provide invaluable information in this area.

In Section 3.1 it was demonstrated that variations in $\alpha_{s,min}$ (the solid fraction below which debris collapses downward) can significantly alter the results of a calculation. Experiments are needed to determine $\alpha_{s,min}$ as a function of the particle diameter (and gluing materials).

Correlations given in Eqs.(3-6) need to be assessed. Of these the residual saturation S_r is the most significant because it determines the time delay between melt formation and relocation. Gravity usually dominates capillary forces in the problems of interest to this study and consequently, variations in P_c do not significantly affect melt relocation. Uncertainties in the permeability κ also have only a small effect.

5. CONCLUSIONS

A two-dimensional model of melt progression in core rubble beds has been developed. The analysis includes mass conservation equations for each species. A two-dimensional (r-z) momentum equation accounts for melt relocation due to both gravity and capillary forces; viscous drag is included by modifying Darcy's Law to account for undersaturated flow, and the wetting behaviour of molten stainless steel in contact with UO_2 is modeled using the formulation suggested by Scheidegger. As solid melts in the center of the bed, the porosity increases; collapse of the bed is incorporated using a critical minimum solid volume fraction $\alpha_{s,min}$. The energy equation considers conduction and radiation heat transfer in the bed, and phase diagrams are used to model Fe-Zr and U-Zr-O interactions.

Solutions are qualitatively similar to the post-accident configuration of the Three-Mile Island (TMI-2) core. Key results are (1) a dense metallic crust is created near the bottom of the bed as molten materials flow downward and freeze; (2) liquid accumulates above the blockage and if Zirconium is present, the pool grows rapidly as molten Zr dissolves both UO_2 and ZrO_2 particles; (3a) if the melt wets the solid, a fraction of the melt flows radially outward under the action of capillary forces and freezes near the radial boundary; (3b) in a nonwetting system, all of the melt flows into the bottom of the bed; and (4) when Zr and Fe are in intimate contact and the Zr atomic fraction is greater than 0.33, these metals can liquefy and flow out of the bed very early in the meltdown sequence.

Oxidation and natural convection effects in the molten pool will be modeled in the near future. Models discussed in this study are being implemented in the MELPROG computer code being developed at Sandia and Los Alamos National Laboratories. The modified version will be used to analyze melt progression, crust growth, pool formation, crust failure and the release of molten materials into the lower plenum during the Three-Mile Island accident. Major uncertainties in the analysis have been identified. Reactor Melt Progression (MP) experiments being planned at Sandia National Laboratories will help resolve some of these uncertainties. Complementary experiments are needed to determine the porosity at which solid collapses as a function of the particle diameter.

REFERENCES

1. S.S. Dosanjh, Ed., MELPROG-PWR/MOD1: A Two-Dimensional, Mechanistic Code for Analysis of Reactor Core Melt Progression and Vessel Attack under Severe Accident Conditions, NUREG/CR-5193, SAND88-1824, Sandia National Laboratories, Albuquerque, NM (to be published).

2. M.F. Young, J.L. Tomkins and W.J. Camp, "MELPROG Code Development and Methods," Proceedings of the International Meeting on LWR Severe Accident Evaluation 1, p.2.8-1, Cambridge, MA (1983).

3. J.E. Kelly, R.J. Henniger and J.F. Dearing, MELPROG-PWR/MOD1 Analysis of a TMLB' Accident Sequence, NUREG/CR-4742, SAND86-2175, Sandia National Laboratories, Albuquerque, NM (1987).

4. M.M. El-Wakil, Nuclear Heat Transport (New York, New York: International Textbook Company, 1971) pp. 94-98.

5. R.J. Lipinski, "A Particle-Bed Dryout Model with Upward and Downward Boiling," Trans. Am. Nuc. Soc. 35, pp. 358-360 (1980).

6. E.L. Tolman, J.P. Adams. J.L. Anderson, P. Kuan, R.K. McCardell and J.M. Broughton, TMI-2 Accident Scenario Update, EGG-TMI-7489, Idaho National Engineering Laboratory, Idaho Falls, ID (1986).

7. D.W. Golden, J.L. Anderson, R.W. Brower, L.J. Fackrell, B.M. Galusha, M.L. Harris, H.E. Knauts, R.D. McCormick, Y. Nomura, C.L. Olaveson, and A. Takizawa, TMI-2 Standard Problem Package, EGG-TMI-7382, Idaho National Engineering Laboratory, Idaho Falls, ID (1986).

8. B.A. Cook and E.R. Carlson, "TMI-2 Core Debris Analysis," CONF-8510166, Proceedings of the First International Information Meeting on the TMI-2 Accident, Germantown, MD (1985).

9. D. Squarer, L.E. Hochreiter and A.T. Pieczynski, "Modes of Heat Removal From a Heat-Generating Debris Bed," Nuclear Technology 65, pp. 16-22 (1984).

10. R.J. Lipinski, "A Review of Debris Coolability Models," Proceedings of the International Meeting on Light Water Reactor Severe Accident Evaluation, Cambridge, MA (1983).

11. R.J. Lipinski, "A Coolability Model For Postaccident Nuclear Reactor Debris," Nuclear Technology 65, pp. 53-66 (1984).

12. E. Gorham-Begeron, "A One Dimensional Time-Dependent Debris Bed Model," ASME/JSME Thermal Engineering Joint Conference, Honolulu, Hawaii (1983).

13. B.D. Turland and K.A. Moore, "One Dimensional Models of Boiling and Dryout," Proc. 5th Post Accident Heat Removal Information Exchange Mtg., Karlsruhe, FRG (1982).

14. B.D. Turland and K.A. Moore, "Debris Bed Heat Transfer with Top and Bottom Cooling," 21st ASME/AIChE Heat Transfer Conference, Seattle WA (1983).

15. J.B. Rivard, Post-Accident Heat Removal: Debris Bed Experiments D-2 and D-3, NUREG/CR-0421, SAND78-1238, Sandia National Laboratories, Albuquerque, NM (1978).

16. J.M. Gronager, M. Schwarz and R.J. Lipinski, PAHR Debris Bed Experiment D-4, NUREG/CR-1809, SAND80-2146, Sandia National Laboratories, Albuquerque, NM (1981).

17. G.W. Mitchell, R.J. Lipinski and M. Schwarz, Heat Removal from a Stratified UO_2-Sodium Particle Bed, NUREG/CR-2412, SAND81-1622, Sandia National Laboratories, Albuquerque, NM (1982).

18. G.W. Mitchell, C.A. Ottinger and R.J. Lipinski, The D7 Debris Bed Experiment, NUREG/CR-3198, SAND82-0062, Sandia National Laboratories, Albuquerque, NM (1983).

19. C.A. Ottinger, G.W. Mitchell, R.J. Lipinski and J.E. Kelly, The D9 Experiment: Heat Removal from Stratified UO_2 Debris in Sodium, NUREG/CR-2951, SAND84-1838, Sandia National Laboratories, Albuquerque, NM (1984).

20. G.W. Mitchell, C.A. Ottinger and H. Meister, The D10 Experiment: Coolability of UO_2 Debris in Sodium With Downward Heat Removal, NUREG/CR-4055, SAND84-1144, Sandia National Laboratories, Albuquerque, NM (1984).

21. C.A. Ottinger, G.W. Mitchell, A.W. Reed and H. Meister, Coolability of Stratified UO_2 Debris in Sodium With Downward Heat Removal: The D13 Experiment, NUREG/CR-4719, SAND86-1043, Sandia National Laboratories, Albuquerque, NM (1987).

22. A.W. Reed, K.R. Boldt, E.D. Gorham-Bergeron, R.J. Lipinski and T.R. Schmidt, DCC-1/DCC-2 Degraded Core Coolability Analysis, NUREG/CR-4390, SAND85-1967, Sandia National Laboratories, Albuquerque, NM (1985).

23. K.R. Boldt, A.W. Reed and T.R. Schmidt, DCC-3 Degraded Core Coolability: Experiment and Analysis, NUREG/CR-4606, SAND86-1033, Sandia National Laboratories, Albuquerque, NM (1986).

24. V.K. Dhir and I. Catton, Study of Dryout Heat Fluxes in a Bed of Inductively Heated Particles, NUREG-0262, University of California at Los Angeles (1977).

25. D. Squarer and J.A. Peoples, "Dryout in Inductively Heated Beds With and Without Forced Flow," Trans. Am. Nucl. Soc. 34, p. 535 (1980).

26. H.C. Hardee and R.H. Nilson, "Natural Convection in Porous Media," Nuclear Science and Engineering 63, pp. 119-132 (1977).

27. D.H. Cho, D.R. Armstrong II and S.H. Chan, "On the Pattern of Water Penetration into a Hot Particle Bed," Nuclear Technology 65, pp. 23-31 (1984).

28. T. Ginsberg, J. Klein, J. Klages and C.E. Schwarz, "Transient Core Debris Bed Heat Removal Experiments and Analysis," International Meeting on Thermal Nuclear Reactor Safety, Chicago, Ill. (1982).

29. D.H. Cho, D.R. Armstrong, L.Bova and S.H. Chan, "Debris Bed Quenching Studies," International Meeting on Thermal Nuclear Reactor Safety, Chicago, Ill. (1982).

30. N.K. Tutu, T.Ginsberg, J. Klein, J. Klages and C.E. Schwarz, Debris Bed Quenching Under Bottom Flood Conditions (In-Vessel Degraded Core Cooling Phenomenology), NUREG/CR-3850, BNL-NUREG-51788, Brookhaven National Laboratory, Upton, N.Y. (1984).

31. T.Ginsberg, J. Klein, J. Klages, C.E. Schwarz and J.C. Chen, LWR Steam Spike Phenomenology: Debris Bed Quenching Experiments, NUREG/CR-2857, BNL-NUREG-51571, Brookhaven National Laboratory, Upton, N.Y. (1982).

32. A.A. Emara and F.A. Kulacki, "A Numerical Investigation of Thermal Convection in a Heat-Generating Fluid Layer," J. Heat Transfer 102, pp. 531-537 (1980).

33. A.J. Suo-Anttila and I. Catton, "The Effect of a Stabilizing Temperature Gradient on Heat Transfer From a Molten Fuel Layer with Volumetric Heating," J. Heat Transfer 102, pp. 544-548 (1974).

34. F.B. Cheung, "Heat Source-Driven Thermal Convection at Arbitrary Prandtl Number," J. Fluid Mech. 97, pp. 743-758 (1980).

35. M. Tveitereid, "Thermal Convection in a Horizontal Fluid Layer with Internal Heat Sources," Int. J. Heat Mass Trasfer 21, pp. 335-339 (1977).

36. F.A. Kulacki and R.J. Goldstein, "Thermal Convection in a Horizontal Fluid Layer with Uniform Volumetric Energy Source," J. Fluid Mech. 55, pp. 271-287 (1972).

37. L. Baker, R.E. Faw and F.A. Kulacki, "Postaccident Heat Removal-Part I: Heat Transfer Within an Internally Heated, Nonboiling Liquid Layer," Nuclear Science and Engineering 61, pp. 222-230 (1976).

38. R.E. Faw and L. Baker, "Postaccident Heat Removal-Part II: Heat Transfer from an Internally Heated Liquid to a Melting Solid," Nuclear Science and Engineering 61, pp 231-238 (1976).

39. J. Morgan, A New Heat Transfer Model for Density Stratified Molten Pools with Internal Heat Sources, CLM-R263, Culham Laboratory, Abingdon, Oxfordshire (1986).

40. H. Kouts, Review of Research on Uncertainties in Estimates of Source Terms from Severe Accidents in Nuclear Power Plants, NUREG/CR-4883, BNL-NUREG-52061, Brookhaven National Laboratory, Upton, New York (April 1987).

41. H.G. Plein and G.A. Carlson, "Debris Bed and Sacrificial Materials Interactions at High Temperatures," Trans. Am. Nucl. Soc. 30, p 436 (1978).

42. H.G. Plein, R.J. Lipinski, G.A. Carlson and D.W. Varela, "Summary of the First Three In-Core PAHR Molten Fuel Pool Experiments," Proc. Int. Mtg. Fast Reactor Safety Technology I, Seattle, WA (1979).

43. D.W. Varela, "High-Temperature Magnesium Oxide Interactions with UO_2," Trans. Am. Nucl. Soc. 34, p. 546 (1980).

44. D.W. Varela, "Molten Steel Behavior in PAHR Debris Beds," Trans. Am. Nucl. Soc. 38, p. 388 (1981).

45. J.T. Hitchcock and J.E. Kelly, "Post-Test Examinations of the In-Pile Molten Pool Experiments," Trans. Am. Nucl. Soc. 43, p. 515 (1982).

46. J.T. Hitchcock and J.E. Kelly, The DC-1 and DC-2 Debris Coolability and Melt Dynamics Experiments, NUREG/CR-4060, SAND84-1367, Sandia National Laboratories, Albuquerque, NM (1985).

47. C.P. Fryer and J.T. Hitchcock, The Postirradiation Examination of the DC Melt Dynamics Experiments, NUREG/CR-4625, SAND86-1102, Sandia National Laboratories, Albuquerque, NM (June 1988).

48. S.S. Dosanjh, On the Melting and Refreezing of Porous Media, NUREG/CR-5028, SAND87-1976, Sandia National Laboratories, Albuquerque, NM (1987).

49. S.S. Dosanjh, On the Melting of Reactor Core Particle Beds, SAND87-2376C, to be presented at the 25th National Heat Transfer Conference, Houston, Texas (1988).

50. S.S. Dosanjh, Melt Progression in Severely Damaged Reactor Cores, NUREG/CR-5029, SAND87-2384, Sandia National Laboratories, Albuquerque, NM (1987).

51. A.E. Scheidegger, The Physics of Flow Through Porous Media, Third Edition (Toronto and Buffalo: University of Toronto Press, 1974) pp. 266-290.

52. C.A. Wert and R.M. Thomson, Physics of Solids, Second Edition (New York, New York: McGraw-Hill Book Co., 1970) pp. 71-72.

53. J. Bear, Dynamics of Fluids in Porous Media (New York, New York: American Elsevier Publishing Company, Inc., 1972) pp. 439-575.

54. F.A.L. Dullien, Porous Media Fluid Transport and Pore Structure (New York, New York: Academic Press, 1979) pp. 251-324.

55. R.A. Greenkorn, Flow Phenomena in Porous Media (New York, New York: Marcel Dekker, Inc., 1983) pp. 112-144,497-530.

56. M.C. Leverett, "Capillary Behavior in Porous Solids," Pet. Trans. AIME 142, pp.152-169 (1941).

57. G.G. Brown and Associates, Unit Operations, Sixth Edition (New York, New York: John Wiley and Sons, Inc., 1956) pp. 210-228.

58. R.B. Bird, W.E. Stewart and E.N. Lightfoot, Transport Phenomena (New York, New York: John Wiley and Sons, Inc., 1960) p. 199.

59. G. Hofmann and L. Barleon, "Reduced Coolability of Particle Beds as a Result of Capillary Effects at Horizontal Phase Boundaries," Proceedings of the International ANS/ENS Topical Meeting on Thermal Reactor Safety, San Diego, California, February 2-6, 1986.

60. J.E. Kelly, J.T. Hitchcock and M.L. Schwarz, "Heat Transfer Characteristics of Dry Porous Particulate Beds with Internal Heat Generation," ASME-JSME Thermal Engineering Joint Conference Proceedings, Honolulu, Hawaii (March 1983).

61. A.V. Luikov, A.G. Shashkov, L.L. Vasiliev and Yu.E. Fraiman, "Thermal Conductivity of Porous Systems," Int. J. Heat Mass Transfer 11, p. 117 (1968).

62. D. Vortmeyer, "Radiation in Packed Solids," Sixth Int. Heat Trans. Conf., Toronto (1978).

63. W. Schote, "Thermal Conductivity of Packed Beds," A.I.Ch.E. Journal 6, p.63 (1960).

64. S. Imura and E. Takegoshi, "Effect of Gas Pressure on the Effective Thermal Conductivity of Packed Beds," Heat Transfer Japanese Research 3, p.13 (1974).

65. M. Hansen, Constitution of Binary Alloys, Second Edition (New York: McGraw-Hill Book Company, 1958) pp. 741-743.

66. D.L. Hagrman, G.A. Reymann and R.E. Mason, MATPRO-Version 11 (Revision 2): A Handbook of Material Properties for Use in the Analysis of Light Water Reactor Fuel Rod Behavior, NUREG/CR-0479, Idaho National Engineering Laboratory, Idaho Falls, ID (1981).

67. D.L. Hagrman, Materials Properties Models for Zirconium-Uranium Oxygen Melting, (PSOL,PLIQ), Solution, and Precipitation (ZUSOLV), Idaho National Engineering Laboratory, Idaho Falls, ID (1985).

68. Reactor Safety Research Semiannual Report January-June 1987 Volume 37, pp. 275-280, NUREG/CR-5039 (1 of 2), SAND87-2411 (1 of 2), Sandia National Laboratories, Albuquerque, NM (1988).

69. J.K. Fink, M.G. Chasanov and L. Leibowitz, Thermodynamic Properties of Uranium Dioxide, ANL-CEN-RSD-80-3, Argonne National Laboratory, Illinois (1981).

70. J.K. Fink, M.G. Chasanov and L. Leibowitz, Transport Properties of Uranium Dioxide, ANL-CEN-RSD-80-4, Argonne National Laboratory, Illinois (1981).

71. J.K. Fink, M.G. Chasanov and L. Leibowitz, Properties for Reactor Safety Analysis, ANL-CEN-RSD-82-2, Argonne National Laboratory, Illinois (1982).

72. D.L. Hagrman, Material Property Models for Severe Core Damage Analysis, EGG-CDD-5801, Idaho National Laboratory, Idaho Falls, ID (1982).

73. R.C. Weast and S.M. Selby, Eds., Handbook of Chemistry and Physics, 48th Edition (Cleveland, Ohio: The Chemical Rubber Co., 1967).

74. C.S. Kim, A. Blomquist, J. Haley, R. Land, J. Fischer, M.G. Chasanov and L. Leibowitz, "Measurement of the Thermal Diffusivity of Molten UO_2," Proceedings of the Seventh Symposium on Thermophysical Properties, Gaithersburg, MD (1977).

75. H.A. Tasman, D. Pel, J. Richter and H.E. Schmidt, "Measurement of the Thermal Conductivity of Liquid Uranium Dioxide," Proceedings of the Eighth European Thermophysical Properties Conference, Baden-Baden, pp. 301-313 (1982).

76. J.K. Fink and L. Leibowitz, An Analysis of Measurements of the Thermal Conductivity of Liquid Urania, ANL-CEN-RSD-83-1, Argonne National Laboratory, Illinois (1983).

77. J.L. Brimhall and J.T. Prater, Heat of Reaction of Molten Zirconium with UO_2, NUREG/CR-4890, PNL-6165, Pacific Northwest Laboratory, Richland, WA (1987).

78. R.W. Ostensen, W.F. Murphy, B.J. Wrona, L.W. Deitrich and J.C. Florek, "Intrusion of Molten Steel into Cracks in Solid Fuel in a Transient-Undercooling Accident in a Liquid-Metal Fast Breeder Reactor," Nuclear Technology 36, pp. 200-214 (1977).

Appendix A

Instabilities in Nonwetting Systems.

In Section 3.2 it was noted that the equations governing melt relocation are very unstable for $90° < \theta < 180°$. An approximate stability analysis follows. Consider undersaturated flow in a porous bed with a uniform solid volume fraction α_s. Melt relocation is governed by Eqs (1,2) in Section 2. Neglecting phase changes, summing Eq.(1) over all species j gives:

$$(1-\alpha_s)\,\frac{\partial S}{\partial t} + \nabla\cdot\,\overline{u} = 0 \quad , \tag{A.1}$$

where it has been assumed that ρ_1 is constant. Equation (2) can be simplified for many applications. It is evident that the time characteristic of changes in velocity is $\kappa_1\rho_1/\mu$. Noting that κ_1 is of the same order as κ, setting d_p=1 mm and α_s=0.6 in Eq.(5), yields $\kappa_1 \simeq 10^{-9}$ m^2. Taking $\mu \simeq 0.005$ Pa•s and $\rho_1 \simeq 7000$ kg/m^3 gives a relaxation time on the order of 10^{-3}s, which is much smaller than the other time scales in the problem. That is, the liquid velocity quickly relaxes to its quasi-steady value

$$\overline{u} = \frac{\kappa_1}{\mu}\left[\,\overline{\nabla}\,P_c - \overline{g}\,\rho_1\right] \quad , \tag{A.2}$$

where ∇P_1 has been replaced by $-\nabla P_c$.

Combining Eqs.(6,A.1 and A.2) gives:

$$\frac{\partial S}{\partial t} - a\,\gamma\cos\theta\;\overline{\nabla}\cdot D_1\overline{\nabla}S - bD_2\;\overline{g}\cdot\overline{\nabla}S = 0 \quad , \tag{A.3}$$

where

$$D_1(S) = S_e^3\,\left|\frac{dJ}{dS}\right| \quad ,$$

$$D_2(S) = S_e^2 \quad ,$$

$$a = \frac{1}{\mu}\left[\frac{\kappa}{1-\alpha_s}\right] ,$$

$$b = \frac{3\rho_1 \kappa}{\mu(1-S_r)(1-\alpha_s)} ,$$

and the Leverett function J depends only on S ($dJ/dS<0$). Note that $S=S_o$ (a constant) is a steady solution of Eq.(A.3). Consider perturbations of the form:

$$S = S_o\left[1 + \epsilon\, e^{i(\omega t-\bar{k}\cdot\bar{r})}\right] , \tag{A.4}$$

where ϵ is a small parameter. Substituting the above expression into Eq. (A.3) and keeping first order terms in ϵ yields:

$$\omega = i\, a'\, \gamma\cos\theta\, |\bar{k}|^2 - b'\, \bar{g}\cdot\bar{k} , \tag{A.5}$$

where $a'=aD_1(S_o)$ and $b'=bD_2(S_o)$. Note that $\mathrm{Im}(\omega)<0$ for $90° < \theta < 180°$ and the perturbation grows exponentially in time. Therefore, in nonwetting systems, solutions are unstable with respect to small perturbations. When the melt wets the solid, $0° < \theta < 90°$, $\mathrm{Im}(\omega)>0$ and solutions are stable. For $\theta=90°$, $\mathrm{Im}(\omega)=0$ and the governing equations are purely hyperbolic.

U.S. Government Printing Office
Receiving Branch (Attn: NRC Stock)
8610 Cherry Lane
Laurel, MD 20707
250 copies for R7

U.S. Nuclear Regulatory Commission (23)
Office of Nuclear Regulatory Research
Division of Reactor System Safety
Washington, DC 20555
Attn: D. Ross
M. Silberberg
G. Marino
C. Kelber
J. Mitchell
R. Meyer
L. Chan
J. Han (5)
P. Worthington
R. Wright (5)
R. VanHouten
B. Burson
T. Walker
P. Wood
T. Lee

U.S. Nuclear Regulatory Commission
Office of Nuclear Reactor Regulation
Washington, DC 20555
Attn: R. Palla

U.S. Department of Energy
Office of Nuclear Safety Coordination
Washington, DC 20545
Attn: R. W. Barber

U.S. Department of Energy (2)
Albuquerque Operations Office
P. O. Box 5400
Albuquerque, NM 87185
Attn: J. R. Roeder, Director
Transportation Safeguards Division
J. A. Morley, Director
Energy Research Technology Division

Argonne National Laboratory
9700 South Cass Avenue
Argonne, IL 60439
Attn: W. Sha

Battelle Columbus Laboratory (2)
505 King Avenue
Columbus, OH 43201
Attn: R. Denning
P. Cybulskis

Battelle Northwest (2)
P. O. Box 999
Richland, WA 99352
Attn: F. Panisko
D. Lanning

Brookhaven National Laboratory (3)
Upton, NY 11973
Attn: R. A. Bari
T. Ginsberg
M. Khatib-Rhabar

Electric Power Research Institute
P. O. Box 10412
Palo Alto, CA 94303
Attn: R. Sehgal (2)

Los Alamos National Laboratory (8)
P. O. Box 1663
Los Alamos, NM 87545
Attn: J. Dearing (5)
E. Fugelso
D. Liles
M. Sahota

Oak Ridge National Laboratory (2)
P. O. Box Y
Oak Ridge, TN 37830
Attn: T. Kress
S. Hodge

EG&G Idaho (4)
P. O. Box 1625
Idaho Falls, ID 83415
Attn: C. Allison
P. Bayless
J. Dahlman
P. Wheatley

University of Wisconsin
Nuclear Engineering Department
1500 Johnson Drive
Madison, WI 53706
Attn: M. L. Corradini

H. Bairiot
Belgonucleaire S. A.
Rue de Champ de Mars 25
B-1050 Brussels
BELGIUM

D. Haas
Belgonucleaire S. A.
Rue de Champ de Mars 25
B-1050 Brussels
BELGIUM

Atomic Energy Canada Ltd. (3)
Chalk River, Ontario
CANADA K0J 1J0
Attn: P. Fehrenbach
M. Notley
D. Nishimura

H. Rosinger
Atomic Energy Canada Ltd.
Pinawa, Manitoba
CANADA ROE 1LO

J. P. Longworth
Central Electric Generating Board
Berkeley Nuclear Labs
Berkeley, Gloucester GL13 9PB
ENGLAND

UK Atomic Energy Authority
SRD
Culcheth, Warrington WA3 4VE
ENGLAND
Attn: M. Hayns
J. Stephenson

UK Atomic Energy Authority (3)
NEEW
Winfrith, Dorchester
Dorset DT2 8DH
ENGLAND
Attn: R. Potter
S. Kinnersley
J. Lillington

B. Turland
UK Atomic Energy Authority
Culham Laboratory
Oxon 0X14 30B
Abingdon
ENGLAND

Kernforschungszentrum (4)
Postfach 3640
7500 Karlsruhe
FEDERAL REPUBLIC OF GERMANY
Attn: A. Fiege
S. Hagen
P. Hoffman
H. Rininsland

G. Petrangeli, Dire R. D. S.
Enea Nucl Energ Alt Disp
Via V Brancati 48
00144 Rome
ITALY

G. Saponaro
Enea Nucl Energ Alt Disp
Via Regina Marg-125
00144 Rome
ITALY

Japan Atomic Energy Res. Inst. (3)
Tokai-Mura Naka-Gun
Ibaraki-Ken 319-11
JAPAN
Attn: K. Hirano
S. Saito
K. Soda

K. J. Brinkmann
Netherlands Energy Res. Fdtn.
P. O. Box 1
1755ZG Petten NH
NETHERLANDS

K. Johansson
Studsvik Energiteknik AB
S-611 82 Nykoping
SWEDEN

J. Bagues
Consejo de Seguridad Nuclear
Sor Angela de la Cruz 3
Madrid 28046
SPAIN

C. Graeslund
Statens Karnkraftinspektion
P. O. Box 27106
S-10252 Stockholm
SWEDEN

Sandia Distribution:

3141	S. A. Landenberger (5)
3151	W. L. Garner
6400	D. J. McCloskey
6415	F. E. Haskin
6418	J. E. Kelly
6420	J. V. Walker
6422	D. A. Powers
6422	W. W. Tarbell
6423	K. O. Reil
6423	R. O. Gauntt
6423	B. W. Marshall, Jr.
6425	W. J. Camp
6425	S. S. Dosanjh (23)
6425	R. D. Gasser
6425	T. J. Heames
6425	A. W. Reed
6425	R. C. Schmidt
6425	R. C. Smith
6425	J. L. Tomkins
6425	K. A. Williams
6425	M. F. Young
6427	M. Berman
6429	K. D. Bergeron
8524	P. W. Dean

NRC FORM 335
(2-84)
NRCM 1102,
3201, 3202

U.S. NUCLEAR REGULATORY COMMISSION

BIBLIOGRAPHIC DATA SHEET

SEE INSTRUCTIONS ON THE REVERSE

1. REPORT NUMBER (Assigned by TIDC, add Vol. No., if any)
NUREG/CR-5109
SAND88-0535

2. TITLE AND SUBTITLE
Relocation of Metallic Constituents in
Core Debris Beds

3. LEAVE BLANK

4. DATE REPORT COMPLETED

MONTH	YEAR
July	1988

5. AUTHOR(S)
S. S. Dosanjh

6. DATE REPORT ISSUED

MONTH	YEAR
September	1988

7. PERFORMING ORGANIZATION NAME AND MAILING ADDRESS (Include Zip Code)
Sandia National Laboratories
Albuquerque, NM 87185

8. PROJECT/TASK/WORK UNIT NUMBER

9. FIN OR GRANT NUMBER
A1342

10. SPONSORING ORGANIZATION NAME AND MAILING ADDRESS (Include Zip Code)
Division of Systems Research
Office of Nuclear Regulatory Research
U.S. Nuclear Regulatory Commission
Washington, DC 20555

11a. TYPE OF REPORT
Technical

b. PERIOD COVERED (Inclusive dates)

12. SUPPLEMENTARY NOTES

13. ABSTRACT (200 words or less)

The MELPROG computer code is being developed to provide mechanistic treatment of Light Water Reactor (LWR) accidents from accident initiation through vessel failure. This paper describes a two-dimensional (r-z) debris meltdown model that has been developed for use in the MELPROG code. Of interest in this study is melt progression in LWR accidents. The analysis includes coupled mass, momentum and energy equations. Phase diagrams are used to model [illegible]-Zr and U-Zr-O interactions. Solutions are qualitatively similar to the post-accident configuration of the Three-Mile Island (TMI-2) core. Key results are (1) a dense metallic crust is created near the bottom of the bed as molten materials flow downward and freeze; (2) liquid accumulates above the blockage and if zirconium is present, the pool grows rapidly as molten Zr dissolves both UO_2 and ZrO_2 particles; (3a) if the melt wets the solid, a fraction of the melt flows radially outward under the action of capillary forces and freezes near the radial boundary; (3b) in a nonwetting system, all of the melt flows into the bottom of the bed; and (4) when Zr and Fe are in intimate contact and the Zr atomic fraction is greater than 0.33, these metals can liquefy and flow out of the bed very early in the meltdown sequence. Major uncertainties in the analysis are identified and validation experiments are discussed.

14. DOCUMENT ANALYSIS - a. KEYWORDS/DESCRIPTORS
Core debris, core meltdown, reactor safety

b. IDENTIFIERS/OPEN ENDED TERMS

15. AVAILABILITY STATEMENT
Unlimited

16. SECURITY CLASSIFICATION
(This page)
Unclassified
(This report)
Unclassified

17. NUMBER OF PAGES

18. PRICE

UNITED STATES
NUCLEAR REGULATORY COMMISSION
WASHINGTON, D.C. 20555

OFFICIAL BUSINESS
PENALTY FOR PRIVATE USE, $300

SPECIAL FOURTH-CLASS RATE
POSTAGE & FEES PAID
USNRC
PERMIT No. G-67

120555139217 1 1AN1R7
US NRC-OARM-ADM
DIV FOIA & PUBLICATIONS SVCS
RRES-PDR NUREG
P-210
WASHINGTON DC 20555

NUREG/CR-5109 RELOCATION OF METALLIC CONSTITUENTS IN CORE DEBRIS BEDS SEPTEMBER 1988